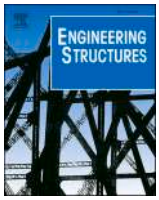
Engineering Structures 371 (2027) 124088



Contents lists available at ScienceDirect

Engineering Structures

journal homepage: www.elsevier.com/locate/engstruct



Experimental and numerical study of flexural behaviour of two-span continuous concrete beams reinforced with hybrid steel and FRP bars: Moment redistribution and serviceability

Ibrahim Abdelhakim, Ali Hassan *, Mahmoud A. Abd-Elaziz, Nesreen M. Kassem, Abdelaziz Nabil

Faculty of Engineering, Tanta University, Egypt

ARTICLE INFO

Keywords:
Concrete
Continuous beams
Moment redistribution
GFRP bars
Hybrid reinforcement

ABSTRACT

Recently, hybrid steel and fiber-reinforced polymer (FRP) bars as tension reinforcement in concrete beams have attracted increasing research interest. To date, several studies have examined the flexural behavior of simple beams with hybrid FRP/steel reinforcement. Until now, limited efforts have focused on continuous beams incorporating such hybrid reinforcement. In the current research, experimental and numerical studies were performed on continuous (two-span) beams subjected to flexural loading. The experimental program included seven beams: one reference beam reinforced with steel bars and six beams with 25%, 50%, and 75% steel-to-GFRP replacement at either the sagging or hogging moment regions. In addition, a finite element study using ABAQUS was conducted to investigate the effects of tension reinforcement ratio, GFRP replacement location, and replacement ratio. The experimental results showed that increasing the GFRP ratio in the sagging region increased deflection and crack width and caused earlier yielding of the remaining steel reinforcement. The steel yield load decreased to 71%, 66%, and 63% of the reference value for replacement ratios of 25%, 50%, and 75%, respectively, while the corresponding beams reached the allowable crack width at 71%, 60%, and 48% of the ultimate load, respectively. In contrast, GFRP replacement in the hogging region had a limited effect on mid-span deflection and ductility but a more pronounced influence on moment redistribution. At 75% replacement, the experimental moment redistribution reached about 8.4% and 17.5% for GFRP replacement at the sagging and hogging regions, respectively. The numerical study further showed that reducing the sagging reinforcement ratio from 1.22% to 0.68% decreased the ultimate load by about 17.5%, while markedly increasing deflection and ductility and promoting greater moment redistribution toward the hogging region, with the ductility index reaching 10.7 and the hogging moment redistribution reaching 30%. Overall, both the location and ratio of GFRP reinforcement significantly influenced the load-carrying capacity, serviceability, ductility, and moment redistribution of continuous concrete beams.

1. Introduction

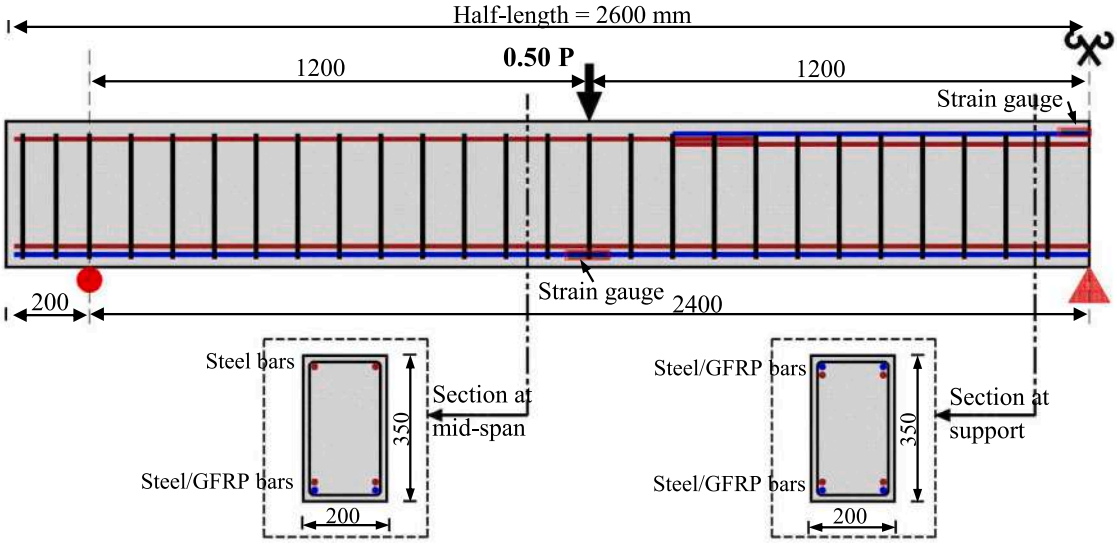
Reinforced Concrete (RC) structures internally reinforced with steel bars have been widely used due to their proven structural efficiency, ductility, and cost-effectiveness. However, the long-term performance of steel-reinforced concrete members is significantly compromised by corrosion of steel reinforcement when exposed to aggressive environmental conditions. Steel corrosion leads to cracking, spalling of concrete cover, reduction in bond strength, and loss of serviceability, which may ultimately result in severe structural deterioration and costly maintenance or replacement works. To overcome these durability-related challenges, fiber-reinforced polymer (FRP) has been used as an alternative to ordinary steel reinforcement owing to its advantages: high tensile strength/weight ratio and excellent resistance to corrosion [1]. Despite these advantages, FRP-reinforced concrete members exhibit several drawbacks, including: linear-elastic behavior till failure; low elastic modulus compared to steel; large deflections; wide crack widths; and brittle failure modes associated with sudden rupture of FRP bars [2–6]. These limitations are particularly critical in statically indeterminate structures, such as continuous beams, where ductility and

* Correspondence to: Structural Engineering Dept, Tanta University, Tanta 31511, Egypt
E-mail address: ali_hassan@f-eng.tanta.edu.eg (A. Hassan).

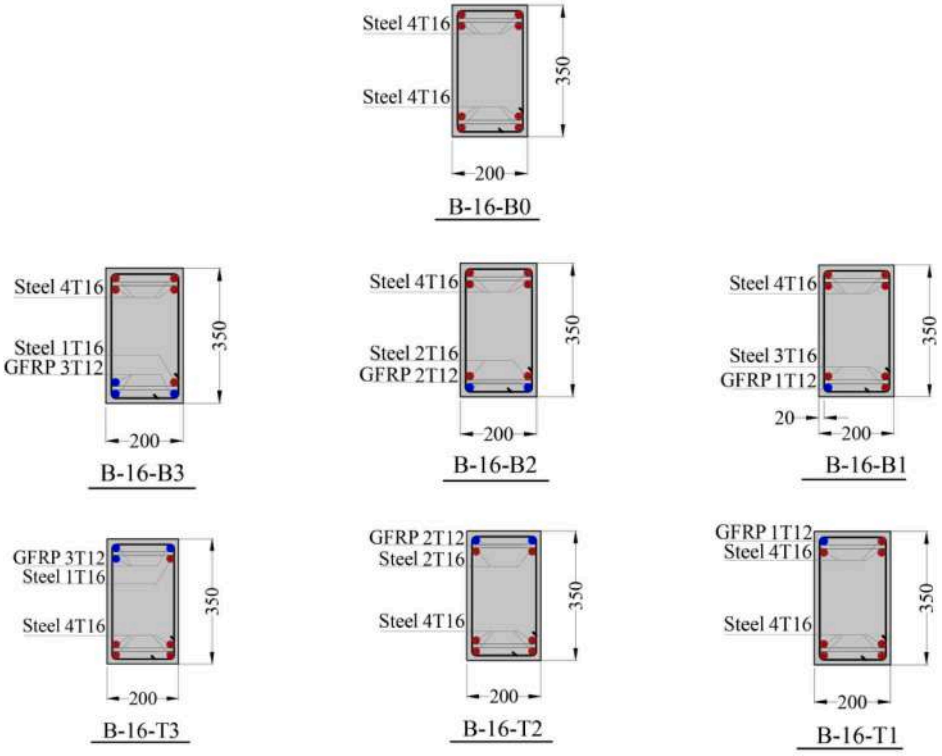
https://doi.org/10.1016/j.engstruct.2026.124088
Received 30 March 2026; Received in revised form 10 September 2026; Accepted 30 October 2026
Available online 3 November 2026
0141-0296/© 2026 Elsevier Ltd. All rights are reserved, including those for text and data mining, AI training, and similar technologies.

moment redistribution play a vital role to ensure structural safety and robustness. Therefore, numerous solutions were proposed to overcome this issue, including the use of hybrid FRP/steel systems and fiber-reinforced concrete. Recent experimental studies have demonstrated that hybrid FRP/steel reinforcement has the ability to improve the flexural stiffness, ductility and serviceability of continuous concrete beams compared to those reinforced by FRP only. However, moment redistribution remains highly dependent on reinforcement ratios and configurations at sagging and hogging regions and may be limited under certain arrangements.

To date, many research has explored the flexural response of simply supported FRP/steel-reinforced beams [7–18]. However, a little work was conducted to figure out the response of continuous onces [19–24]. Araba et al. [19] tested two-span beams with steel/GFRP bars, focusing on the effect of tension reinforcement ratio (μ_t). The tests revealed improved ductility and load capacity in the hybrid reinforced beams compared to those with FRP only. The moment redistribution was limited when similar reinforcement layouts were used [19]. Araba and Ashour [20] evaluated the behaviour of two-span beams with combinations of steel and GFRP. The study revealed that better stiffness could be achieved at the post-cracking stages with the use of hybrid bars. Almahmood et al. [21] reported a flexural study of continuous RC beams



a. General reinforcement details.



b. {ross-sectional details of the experimental beams at the mid-support.

Fig. 1. Details of the tested beams (all dimensions in mm).

strengthened with hybrid steel/GFRP reinforcement and concluded improved stiffness, crack control, and serviceability performance compared to GFRP-only beams. At the same time, moment redistribution at failure remained restricted owing to the early steel yielding. Akiel et al. [22] examined the behaviour of continuous concrete beams reinforced with hybrid steel/BFRP bars and found that the hybrid reinforcement reduced the deflections and crack width at all loads. In addition, the redistribution capacity was strongly dependent on the hogging-to-sagging reinforcement ratio.

As noted in the previous review, most of the earlier studies were carried out on continuous concrete beams with hybrid FRP/steel bars at both sagging and hogging moment regions at the same time. However, to the authors' knowledge, limited research has examined the behaviour of those with hybrid bars applied at either sagging or hogging regions. Two-span continuous beams were selected because their statically indeterminate behaviour makes moment redistribution sensitive to stiffness changes in the sagging and hogging regions. Such beams are commonly encountered in multi-span RC structural systems, where GFRP reinforcement may be beneficial, particularly under aggressive environmental conditions. Therefore, the main contribution of this study is the selective use of hybrid steel/GFRP reinforcement at either the sagging or hogging moment regions of two-span continuous beams, allowing the effects of the reinforcement location on both serviceability and moment redistribution to be assessed experimentally and numerically. In this study, seven two-span RC beams were tested under flexural loads. The tests included: one reference beam with traditional steel bars at both sagging and hogging regions, and six with hybrid steel/GFRP bars implemented only in the sagging or only in the hogging moment regions. When the hybrid bars were used, different replacement ratios of GFRP were studied. For in-depth analysis of the test results, the results were presented in terms of failure modes, load-deflection relationship, ductility analysis, reinforcement strains, visual crack width measurements, plastic/elastic support reactions, moment redistribution, and moment capacity. Additionally, a finite element analysis was performed on selected specimens with varying reinforcement ratios and GFRP replacement locations to further explore their structural behaviour and to support the experimental findings.

2. Experimental work

2.1. Description of the beams

In the experimental work, seven two-span concrete beams with identical dimensions were fabricated and tested. Fig. 1 shows the description of the beams. As shown in the Figure, the total length, effective span length, width and depth of the beams were 5200, 2400, 200 and 350 mm, respectively. The steel stirrups were identical in all beams. Stirrups with 10 mm diameter were distributed over the entire beam at an equal spacing of 100 mm. For longitudinal reinforcement, all beams were reinforced at tension zones with four longitudinal bars, either steel or hybrid bars combining steel and GFRP bars. In the compression zones, two steel bars of 12 mm diameter were reinforced with an overlap of 250 mm with the hogging reinforcement.

Table 1 presents the tested beams in the experimental study. A total of seven beams were tested. For comparison with traditional steel reinforcement, one reference beam (B-16–0) was reinforced with four steel bars of 16 mm diameter at both negative (hogging) and positive (sagging) moment regions. Whereas, the reimaging beams were reinforced with hybrid GFRP/steel bars at either sagging of hogging moment. The main test variables were the location of the hybrid reinforcement and the GFRP/steel replacement ratio. For group 1, composed of 3 specimens, different ratios of steel bars were replaced by equivalent GFRP bars at the sagging moment regions. As for the beams of group 2, composed of 3 specimens, different ratios of steel bars were replaced by equivalent GFRP bars at the hogging moment region. In the hybrid reinforced regions, either one, two, or three of the steel bars at the tension zone were replaced by equivalent GFRP bars, representing replacement ratios of 25, 50 and 75% of the total reinforcement. Instead of each steel bar with 16 mm diameter, a ribbed GFRP bar with 12 mm diameter was used. The alternative GFRP bar had almost a similar

Table 1
Test parameters for experimental and numerical study.

Hogging reinforcement		Sagging reinforcement		Beam notation	Group No.	Study
GFRP ($\rho_{f\ \%}$)	Steel ($\rho_{s\ \%}$)	GFRP ($\rho_{f\ \%}$)	Steel ($\rho_{s\ \%}$)			
-	4T16 (1.22)	-	4T16 (1.22)	B-16–0	Control	Experimental and Numerical
-	4T16 (1.22)	1T12 (0.17)	3T16 (0.91)	B-16-B1	Group 1	
-	4T16 (1.22)	2T12 (0.34)	2T16 (0.61)	B-16-B2		
-	4T16 (1.22)	3T12 (0.51)	1T16 (0.30)	B-16-B3		
-	4T16 (1.22)	4T12 (0.68)	-	*B-16-B4		
1T12 (0.17)	3T16 (0.91)	-	4T16 (1.22)	B-16-T1	Group 2	
2T12 (0.34)	2T16 (0.61)	-	4T16 (1.22)	B-16-T2		
3T12 (0.51)	1T16 (0.30)	-	4T16 (1.22)	B-16-T3		
4T12 (0.68)	-	-	4T16 (1.22)	*B-16-T4		
-	4T16 (1.22)	-	4T12 (0.68)	B-12-B0	Group 3	Numerical
-	4T16 (1.22)	1T8.5 (0.09)	3T12 (0.51)	B-12-B1		
-	4T16 (1.22)	2T8.5 (0.17)	2T12 (0.34)	B-12-B2		
-	4T16 (1.22)	3T8.5 (0.26)	1T12 (0.17)	B-12-B3		
-	4T16 (1.22)	-	4T20 (1.90)	B-20-B0	Group 4	
-	4T16 (1.22)	1T14 (0.23)	3T20 (1.43)	B-20-B1		
-	4T16 (1.22)	2T14 (0.47)	2T20 (0.95)	B-20-B2		
-	4T16 (1.22)	3T14 (0.70)	1T20 (0.48)	B-20-B3		
-	4T12 (0.68)	-	4T16 (1.22)	B-12-T0	Group 5	
1T8.5 (0.09)	3T12 (0.51)	-	4T16 (1.22)	B-12-T1		
2T8.5 (0.17)	2T12 (0.34)	-	4T16 (1.22)	B-12-T2		
3T8.5 (0.26)	1T12 (0.17)	-	4T16 (1.22)	B-12-T3		
-	4T20 (1.90)	-	4T16 (1.22)	B-20-T0	Group 6	
1T14 (0.23)	3T20 (1.43)	-	4T16 (1.22)	B-20-T1		
2T14 (0.47)	2T20 (0.95)	-	4T16 (1.22)	B-20-T2		
3T14 (0.70)	1T20 (0.48)	-	4T16 (1.22)	B-20-T3		
1T12 (0.17)	3T16 (0.91)	1T12 (0.17)	3T16 (0.91)	B-16-BT1	Group 7	
2T12 (0.34)	2T16 (0.61)	2T12 (0.34)	2T16 (0.61)	B-16-BT2		
3T12 (0.51)	1T16 (0.30)	3T12 (0.51)	1T16 (0.30)	B-16-BT3		

ρ_s = Steel reinforcement ratio; ρ_f = GFRP reinforcement ratio, * Numerical model only

tensile strength capacity, where the tensile capacity (Area of bar, mm^2 × tensile strength, MPa) of the steel bar of 16 mm diameter and the GFRP bar of 12 mm diameter were 104,520 and 107,350 N, respectively. A similar tensile-capacity-based approach has also been adopted in previous experimental studies on steel–GFRP reinforced continuous beams [20]. It should be noted that the sections were designed to reach a steel yielding pattern before failure. Fig. 2 shows the design boundaries of the expected failure modes for FRP/steel reinforced sections [25]. As shown in this figure, the reinforcement ratios of the studied beams lie between the governing boundaries of the tension failure mode.

2.2. Material properties

2.2.1. Concrete

The used concrete patch was supplied by a commercial ready-mix plant with a target cylindrical compressive strength of 28 MPa. The proportions of the used mixture are presented in Table 2. In this mixture, normal-strength Portland cement (CEM 42.5), fine river sand (grain size = 0.3–0.5 mm), crushed limestone (N.M.S. = 20 mm), and tap water were used. As per ASTM C39/C39M [26], six cylinders (L×d = 300 ×150 mm^2) were sampled to measure the actual strength. The tests of the cylinders were carried out at the same date of the beams'. The actual compressive strength ($f_c^{'}$) was about 30.8 MPa. Also, indirect tensile tests were carried out on six cylinders (L×d = 300 ×150 mm^2). The average tensile strength (f_{ct}) was 2.95 MPa.

2.2.1.1. Steel reinforcement. As presented in Section 2.1, ribbed steel bars with different diameters of 10, 12, and 16 mm were used. Following the specification of ASTM E8/E8M [27], the uniaxial tensile tests were carried out on three samples of each diameter. Table 3 summarizes the test outputs. As presented in Table 3, the yield strengths (f_y) of the bars of 10, 12, and 16 mm were 510, 513, and 520 MPa, respectively. Where the ultimate strengths (f_{ult}) of the bars of 10, 12, and 16 mm were 635, 650, and 670 MPa, respectively.

2.2.1.2. GFRP reinforcement. Ribbed GFRP bars were used instead of the steel bars at the tension side. Following ACI440.3 R-15 [1], three samples were tested to measure the tensile properties of the GFRP bars. Fig. 3 shows the details of the uniaxial tensile test. During the test, the stress concentration at the grips of the universal machine may lead to a premature failure of the tested bars. Thus, as shown in Fig. 3, the ends of the bars were embedded through a hollow steel tube of 16 mm diameter, and then the tube was filled with epoxy adhesive. Fig. 3 and Table 3 show the properties of the used GFRP. The maximum tensile strength (f_{ult}) and Young's modulus (E_f) of the GFRP bars were 950 MPa and 55 GPa, respectively.

2.3. Test setup

Fig. 4 presents the arrangement of the setup. As shown in Fig. 4, each beam consisted of two equal spans (L_f = 2400 mm). During the test, the beam was placed over a roller support at each end and a hinged support at the specimen's mid-length. Employing a consistent loading rate of 10 kN/min, the load was applied through a hydraulic jack with a load capacity of 2000 kN. As shown in the test setup, a stiff steel beam was used to transmit the load to the midpoint of each span. Two calibrated load cells were used to measure the acting load and the reaction of the middle support. To measure the developed deformations, six linear variable displacement transducers (LVDTs) were placed under the beam to measure the developed deflection. Also, three LVDTs were placed at the supporting points to measure any possible deformation. At the points of maximum tensile strain of both the sagging and hogging moments, electrical strain gauges (6 mm gauge length) were bonded on the tension steel/GFRP bars to measure the strain. The measuring devices were linked to a data logger with 20 channels and the results were monitored through a laptop connected to the data logger.

3. Test results

3.1. Loads and mode of failure

Fig. 5 shows a sketch of the typical cracking pattern of the continuous beams and images of the final cracking pattern obtained from the experimental study. Table 4 lists the loads at first crack, yield, and failure of the beams. For the control beam, the first flexural crack appeared in the hogging zone at a load of 74 kN. Subsequently, the first flexural crack was noticed in the sagging zone at a load of 87 kN. The primary cracks (flexural cracks) initiated vertically, perpendicular to the beam axis. Increasing the applied load, new flexural shear cracks were observed away from the maximum moment zones. In the sagging moment, the initiated flexural shear cracks extended in an inclined direction toward the load location, while at the hogging moment, the cracks extended in an inclined direction toward the middle support. At a load of 614 kN, the beam failed, exhibiting a flexural shear pattern after reaching the yield state of the steel bars at the sagging and hogging moments. The beams of groups 1 and 2 exhibited the same cracking pattern and mode of failure as the control beam. The first flexural cracks of the beams appeared at the hogging and sagging moments,

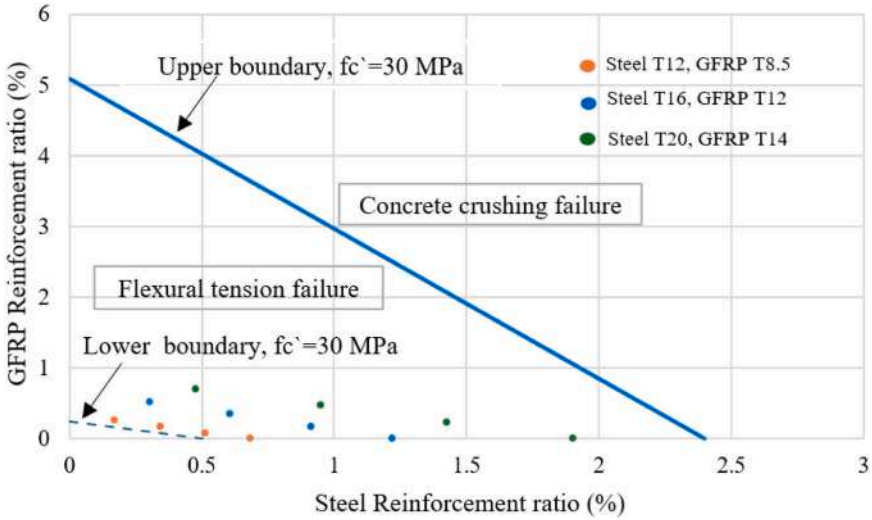


Fig. 2. Failure boundaries for different GFRP and steel reinforcement combinations.

Table 2
Concrete mix proportions.

Designed concrete mixure	Cement, kg/m^3	Sand, kg/m^3	Crushed stone, kg/m^3	Water, kg/m^3	Superplasticzer, kg/m^3	W/C
Mixure	400	600	1010	200	___	0.50

Table 3
Properties of GFRP and steel reinforcement.

Type of bars	Diameter, mm	Yield Strength, MPa	Ultimate Strength, MPa	Modulus of Elasticity, GPa
Longitudinal GFRP	12	N/A	950	55
Longitudinal steel	16	520	670	200
	12	513	650	200
Steel stirrups	10	510	635	200

corresponding to average loads of 71 and 83, respectively. At the peak load, the beams failed in a similar pattern (flexural shear failure) after yielding of the internal steel reinforcement at the sagging and hogging moments without rupture of the GFRP bars. As shown in Table 4, B-16-B1, B-16-B2, and B-16-B3 achieved loads of 585, 583, and 580 kN, respectively. B-16-T1, B-16-T2, and B-16-T3 achieved loads of 622, 620, and 616 kN, respectively. As expected, the ultimate load results match the design philosophy of the study, as the beams were designed to achieve nearly similar capacities.

3.2. Load deflection response

Fig. 6 plots the load deflection results of the beams. The allowable service deflection for the beams is included in the figure, which corresponds to 9.6 mm for the studied beams, as per ACI 318–19 [28]. The relatively small differences between the load-deflection curves are partly attributed to the adopted replacement criterion, as the steel and GFRP bars were selected to provide approximately similar tensile capacities. Therefore, increasing the GFRP replacement ratio had a limited effect on the load-carrying capacity. However, due to the lower elastic modulus of GFRP, its influence became more evident after cracking through changes in the flexural stiffness and deflection response. Fig. 7 depicts an idealization for load deflection curves of continuous beams with hybrid reinforcement versus those with steel bars [19]. Generally, as shown in Figs. 6 and 7, the load deflection of the tested beams can be divided into three sequential stages. For the control beam, stage one

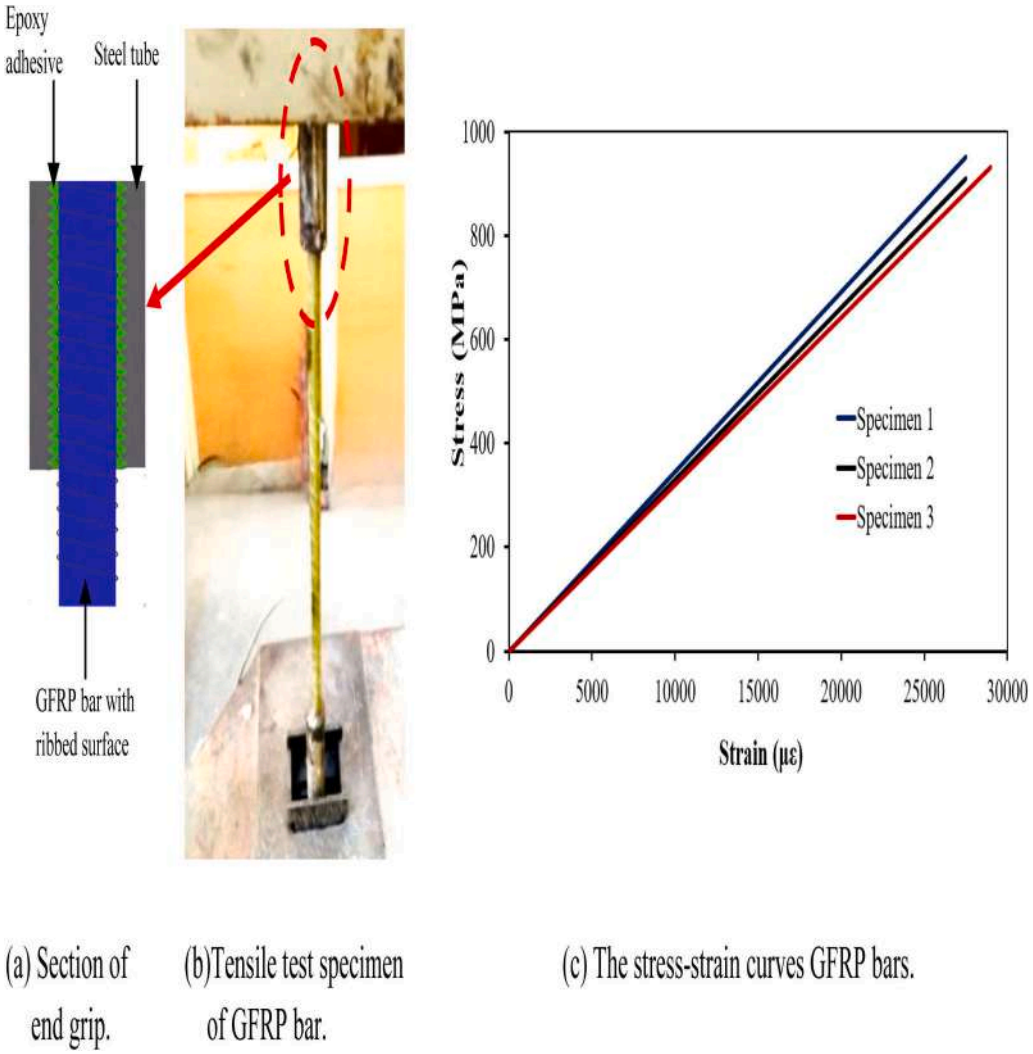


Fig. 3. Uniaxial tensile test for the used GFRP bars.

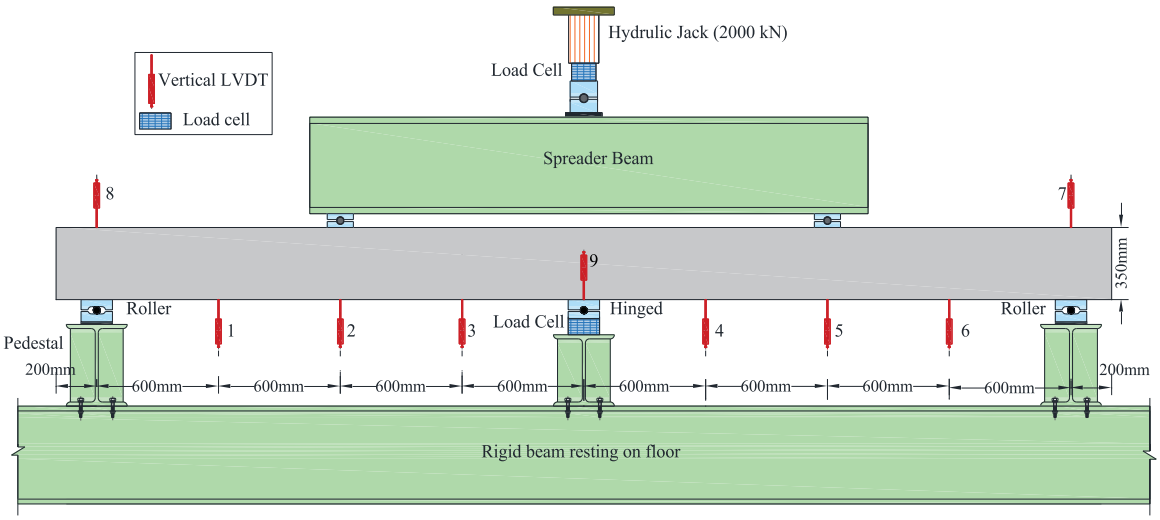


Fig. 4. Test setup and instrumentation.

(elastic stage) started from the initial loading till the first cracking load. Beyond this, at the following stage (elastoplastic stage), the initiation of the cracks led to a noticeable reduction in the beam stiffness. This stage ended when the tension steel reinforcement reached the yield state. Lately, at stage three (plastic stage), the deflection increased dramatically with a negligible increase in the load until failure. At failure, the beam achieved a maximum deflection of 36 mm.

Group 1 had hybrid reinforcement at the sagging moment regions. As shown in Fig. 6a, only the first stage in group 1 was almost identical to the control beam. Whereas at the second stage, increasing the percentage of the GFRP at the expense of steel reinforcement decreased the flexural stiffness of the beams and then increased the developed deflection. For instance, when the beams reached the allowable value of the service deflection, the beams gained loads of 498, 457, and 415 kN for beams B-16-B1, B-16-B2, and B-16-B3, respectively. The achieved values represent 95, 87, and 79% of that of the control beam. Also, at stage three, starting from the yielding of the tension steel up to failure, the beams demonstrate a deflection hardening response after the yield of the steel reinforcement. Moreover, as presented in Fig. 6a, the slope of the post-yield deflection (post-yield stiffness) increased with increasing the GFRP ratio. Where the control beam didn't achieve a post-yield stiffness. In contrast, the post-yield stiffness of B-16-B1, B-16-B2, and B-16-B3 were 10, 11.8 and 15 kN/mm, respectively. However, the hybrid reinforcement in the sagging moment region decreased the achieved ultimate deflection, which decreased with increasing the GFRP ratio. At failure, the maximum deflections of B-16-B1, B-16-B2, and B-16-B3 were 32, 30.5, and 29.5 mm, respectively. The obtained values represent 89, 83, and 82% of that achieved by the control beam.

Group 2 had hybrid reinforcement in the hogging moment region. As shown in Fig. 6b, the use of hybrid reinforcement in the hogging moment region at the expense of steel reinforcement has a lower effect on the load deflection response. At all stages, the beams of hybrid reinforcement showed a similar behaviour to that of the control beam. For instance, B-16-T1, B-16-T2, and B-16-T3 reached the service deflection at almost similar loads, which were 522, 520, and 516 kN, respectively. These values represent 99.6, 99.2, and 98% of that achieved by the control beam. This behaviour can be attributed to the constant flexural stiffness at the sagging moment. Moreover, at the last stage, a slight change in the post-yield stiffness was observed with increasing the GFRP ratio. For instance, the post-yield stiffness of B-16-T1, B-16-T2 and B-16-T3 are 9.18, 10, and 10.2 kN/mm, respectively. At failure, the maximum deflection of B-16-T1, B-16-T2, and B-16-T3 were 35, 35, and 34 mm, respectively.

3.3. Ductility measurements

3.3.1. Deflection-based ductility (μ_Δ)

The deflection-based ductility index (μ_Δ) is the ratio of the deflection at ultimate (Δ_u) to that of the first yield load (Δ_y). The first yielding may occur either at the tension side of the sagging or in the hogging, based on the pattern of the reinforcement. Table 4 presents the calculated indices (μ_Δ) for the beams. As shown in Table 4, the control beam achieved the highest value compared to the tested beams, achieving a ductility index of 5.8. For group 1, the use of hybrid bars at the sagging moment showed a decrease in the ductility index. In addition, the loss increases with increasing the GFRP ratio. The ductility indices of B-16-B1, B-16-B2, and B-16-B3 were 5.7, 4.9, and 4.0, respectively. These values represent 98, 84.5, and 69% of that achieved by the control beam. As for group 2, the hybrid reinforcement at hogging moment showed a lower effect on ductility compared to group 1. The ductility indices of beams B-16-T1, B-16-T2, and B-16-T3 were 5.75, 5.5, and 4.95, respectively. These values represent 1, 12.5, and 23.8% higher than those achieved by their counterparts in group 1.

3.3.2. Energy-based ductility

The ductility of the beams was additionally evaluated based on the absorbed energy. The energy index (μ_E) is the ratio of the total energy (E_{total}) to the elastic energy ($E_{Elastic}$), and can be obtained by Eq. (1) [7]. Fig. 8 shows the parameters E_{total} and $E_{Elastic}$ of the energy-based ductility. Table 4 presents the results of the energy ductility indices (μ_E) for the tested beams.

$$\mu_E = \frac{1}{2}\left(\frac{E_{total}}{E_{elastic}} + 1\right) \quad (1)$$

As shown in Table 4, the energy-based approach results closely match those of the deflection-based ductility. The control beam recorded the highest energy index among the tested beams, with a value of 6.14. For group 1, applying hybrid bars at the sagging moment region decreased the energy-based index. The indices for B-16-B1, B-16-B2, and B-16-B3 were 6.03, 4.5, and 3.2, respectively, representing 98%, 73%, and 52% of the control beam (B-16–0). In group 2, using hybrid reinforcement at the hogging moment had a lesser effect on the energy index compared to group 1. The energy-based indices for B-16-T1, B-16-T2, and B-16-T3 were 6.1, 5.9, and 4.7, respectively, which are 1.2%, 31%, and 46% higher than their counterparts in group 1. Overall, the analysis indicates that hybrid reinforcement at the sagging moment has a more significant impact on ductility than reinforcement at the hogging moment.



Fig. 5. Crack pattern for the tested beams.

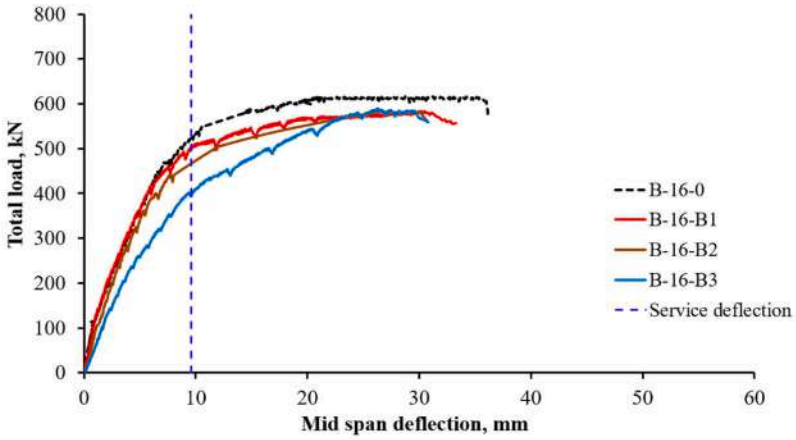
Table 4
Summary of test results.

Beam notation	At the first flexural crack at sagging		At the first flexural crack at hogging		At the yield load of steel at sagging		At the yield load of steel at hogging		At the ultimate load		μ_Δ	μ_E
	P_{cr}, kN	Δ_{cr}, mm	P_{cr}, kN	Δ_{cr}, mm	P_{ys}, kN	Δ_y, mm	P_{yh}, kN	Δ_y, mm	P_{ult}, kN	Δ_{ult}, mm		
B-16–0	87	2.3	74	1.5	495	9.6	480	6.2	614	36	5.8	6.14
B-16-B1	85	2.2	71	1.3	350	5.6	460	8.8	585	32	5.7	6.03
B-16-B2	86	2.9	71	1.25	325	6.2	445	10.4	583	30.5	4.9	4.5
B-16-B3	83	3.05	69	1.4	310	7.2	428	11	580	29.5	4	3.2
B-16-T1	82	1.6	72	1.35	490	9	440	6.1	622	35	5.75	6.1
B-16-T2	80	1.9	72	1.6	478	9.5	420	6.4	620	35	5.5	5.9
B-16-T3	78	2	70	1.45	445	9.5	408	6.9	616	34	4.95	4.7

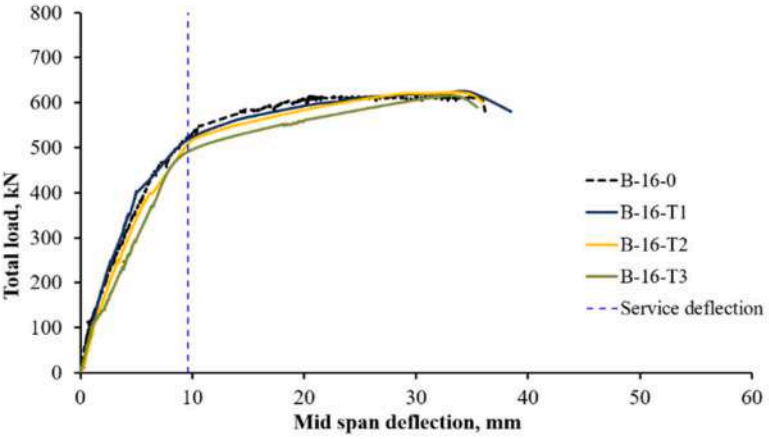
P_{cr} = first crack load; P_{ys} = yield load for sagging steel; P_{yh} = yield load for hogging steel; P_{ult} = ultimate load; Δ *the deflection at sagging;* Δ_{cr} = deflection at cracking load; Δ_y = deflection at yield load; Δ_{ult} = deflection corresponding to ultimate load; μ_Δ=ductility index = Δ_{ult}/Δ_y; μ_E =energy ductility index.

3.4. Tensile reinforcement strain

Fig. 9 plots the load versus the tensile strain at the mid-span. The yield strain limit ($\varepsilon_y = 2600\ \mu\varepsilon$) is presented in the figures. It should be noted that when combinations of steel and GFRP bars were used, strain gauges were bonded to each. At the same load level, the strain readings

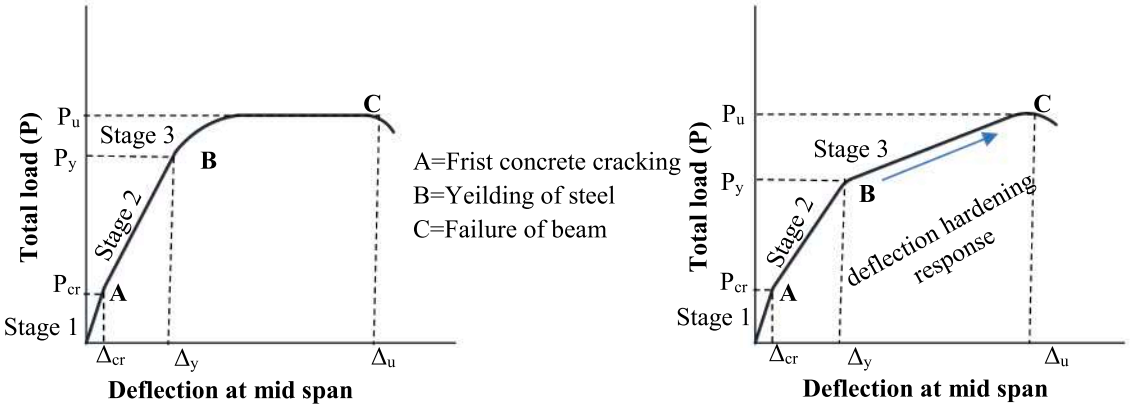


(a) Load versus mid-span deflection for the beams of group 1.



(b) Load versus mid-span deflection for the beams of group 2.

Fig. 6. Load versus mid-span deflection for all tested beams.



(a) Beams with steel reinforcement (b) Beams with FRP/steel reinforcement

Fig. 7. Typical load deflection curves for hybrid and steel reinforced beams [19].

were almost similar in both steel and GFRP bars, owing to section strain compatibility. As shown in Fig. 9, the control beam showed an elastic-plastic strain response, and the beam reached the yield strain at a load of 495 kN. Fig. 9a shows the strain response of tensile reinforcement at the sagging moment. As indicated in Fig. 9a, the use of GFRP bars instead of steel increased the developed strain, especially at the post-

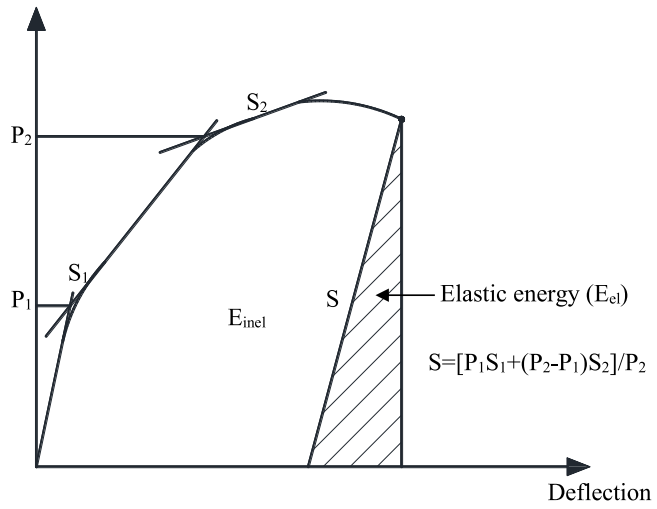


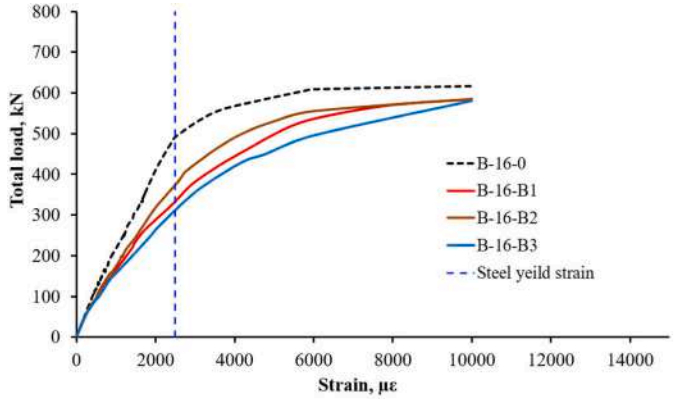
Fig. 8. Total, elastic and inelastic energies.

cracking stage. This behaviour is attributed to the lower elastic modulus of GFRP, which is approximately 25% of steel. Therefore, increasing the GFRP replacement ratio reduced the stiffness contribution of the tension reinforcement after cracking, resulting in higher tensile strains and earlier yielding of the remaining steel reinforcement. Beams B-16-B1, B-16-B2 and B-16-B3 reached the yield state at loads of 350, 325 and 310 kN, respectively. The values are 71, 66, and 63% of that achieved by beam B-16–0 (the control beam).

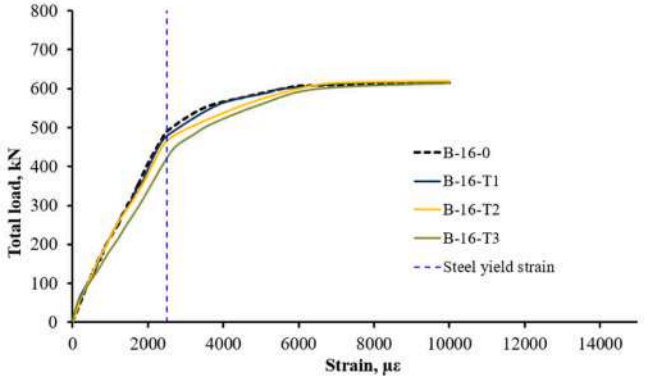
Fig. 10 plots the load versus the tensile strain at the hogging moment region. As indicated in the Figure, similar to group 1, when the hybrid bars were used at the hogging moment, the developed strain increased. Beams B-16-T1, B-16-T2, and B-16-T3 reached their yield strain at loads of 440, 420, and 408 kN, respectively. These values are 92, 87, and 85% of that achieved by B-16–0. This gradual reduction in the yield load with increasing GFRP replacement ratio can be attributed to the lower stiffness of the hybrid reinforcement in the hogging region. The effect was less noticeable than that observed for the sagging replacement, since the sagging region remained fully reinforced with steel bars.

3.5. Load crack width response

Fig. 11 plots the maximum crack width for the tested beams. As per ACI 318–19 [28], the allowable crack width in the case of ordinary exposed structures is 0.3 mm, which is included in the figure for comparison. Comparing the results of the beams, the control beam showed a controlled crack width till reaching about 460 kN, at which the internal steel reinforcement reached the yield state. Beyond this, an obvious increase in the crack width readings was observed. In the hogging moment region, the beam reached the allowable crack width at approximately 500 kN; this value represents 81% of its ultimate load (P_u). This ensures the serviceability requirements, as the service load of

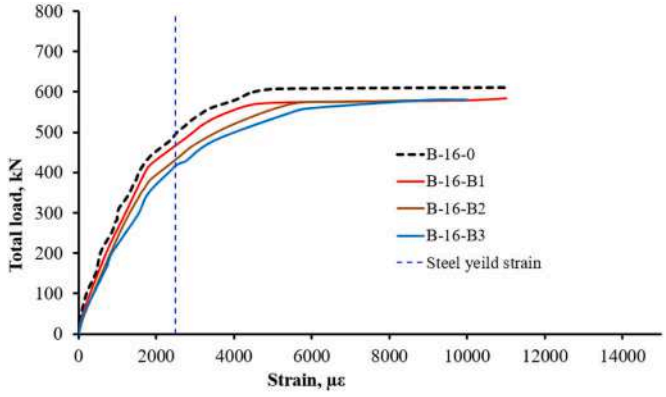


(a) Load-steel strain curves of group 1 at the sagging moment.

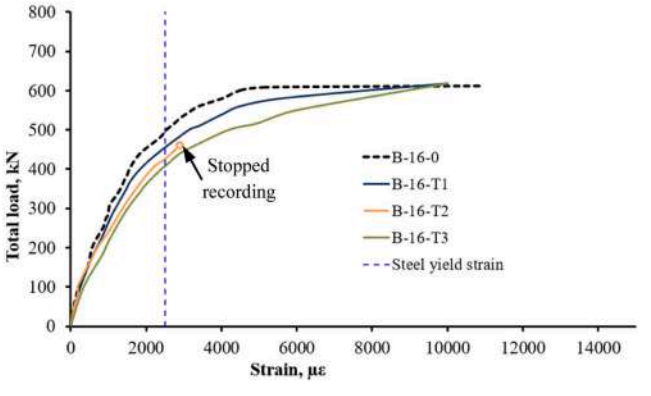


(b) Load-steel strain curves of group 2 at the sagging moment.

Fig. 9. Load versus strain curves for the tested beams at the sagging moment.



(a) Load-steel strain curves of group 1 at the hogging moment.



(b) Load-steel strain curves of group 2 at the hogging moment.

Fig. 10. Load versus strain curves for the tested beams at the hogging moment.

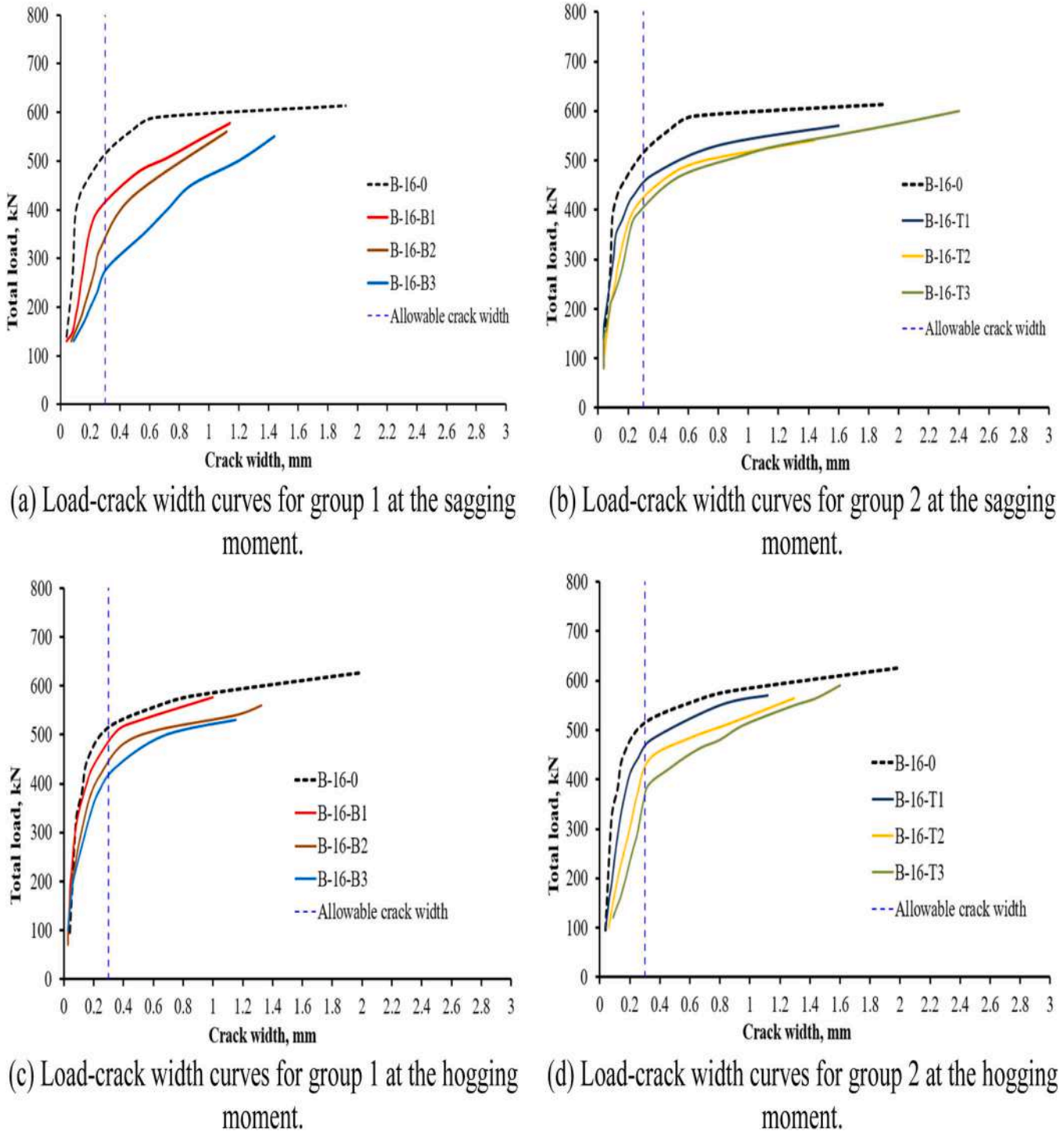


Fig. 11. Crack width of tested beams.

the beam is 0.67 P_u, according to ECP-203 [29]. For group 1, as shown in Fig. 11a, a noticeable increase in the crack width readings at the sagging moment region was observed, where the hybrid bars were used. While a slight increase in crack width was observed at the hogging moment. At the sagging moment region, B-16-B1, B-16-B2, and B-16-B3 reached the allowable crack width at 420, 350 and 280 kN, respectively. These values represent 0.71 P_u, 0.60 P_u, and 0.48 P_u, respectively. This indicates a great drop in the serviceability requirements, especially for beams B-16-B2 and B-16-B3, as their loads were lower than 0.67 P_u. As for group 2, as shown in Fig. 11b, the use of hybrid bars in the hogging moment region had a lower impact on the measured crack width compared to the results of group 1. Beams B-16-T1, B-16-T2, and B-16-T3 reached the allowable crack width at the hogging moment region at loads 480 kN, 450 and 390 kN, respectively. These values represent 0.77 P_u, 0.72 P_u, and 0.63 P_u, respectively. The increase in crack width with increasing GFRP replacement ratio is mainly attributed to the lower elastic modulus of GFRP, which results in higher tensile strains and wider cracks after cracking. This effect was more significant when the GFRP bars were used in the sagging region.

3.6. Redistribution of support reactions

For all beams, the reaction at the middle support was recorded throughout the experimental test using a 500 kN load cell, as indicated in Fig. 4. Furthermore, the symmetry of the beam geometry and loading arrangement led to equal reactions at the end supports. Fig. 12 shows the typical stages of end reaction. Stage one started from the initial loading up to the first crack load. Following, stage two started, which extended to the yielding of the steel reinforcement. Finally, stage three, which extended from the yielding of the steel reinforcement up to failure. Figs. 13 and 14 show the end support reactions plotted versus the total load for the beams. For comparison, the elastic reaction (R = 0.319 P) was calculated from the uncracked beam analysis and included in the Figures. As expected, in stage one (uncracked stage), the measured reaction of the beams was congruent with the calculated ones. The beams showed a noticeable redistribution of reaction after cracking, indicating a redistribution of moment between the sagging and hogging regions. For the control beam, in stage two, the results showed that the end support reaction was slightly higher than the elastic prediction, indicating the redistribution of load from the hogging to the sagging moment. Moreover, in the third stage, the results showed a similar trend; however, a higher rate of increase was observed. For group 1, in stage two, the end support reaction was lower than the elastic prediction, as shown in Fig. 13, indicating a redistribution of load from the sagging to the hogging moment. This is as a result of higher stiffness in the hogging moment (with steel reinforcement). Beyond this, in stage 3, the redistribution of load started to decrease, indicating the increased contribution of the GFRP at sagging after reaching the yield state of the steel reinforcement. With increasing GFRP replacement ratio, the stiffness of the sagging region decreased relative to the fully steel-reinforced hogging region, resulting in greater load redistribution from the sagging to the hogging region. For group 2, in stage two, the end support reaction was higher than the elastic prediction, indicating a redistribution of load from the hogging to the sagging moment as a result of higher stiffness in the sagging moment. Thereafter, in stage three, the redistribution of load started to decrease, indicating the increased contribution of the GFRP at hogging after the yielding of the steel reinforcement. Similarly, increasing the GFRP replacement ratio reduced the stiffness of the hogging region relative to the fully steel-reinforced sagging region, resulting in greater load redistribution from the hogging to the sagging region.

3.7. Moment redistribution

The drawings of the moment redistribution (M.R) at ultimate are presented in Fig. 15. The values of the moment redistribution are obtained by the following equation (Eq. 2).

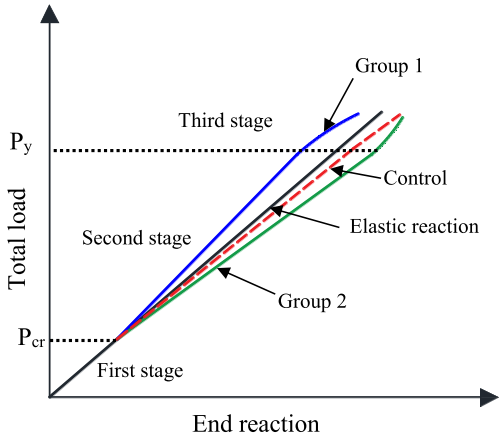


Fig. 12. Typical stages of end support reactions.

$$M.R = \frac{M_p - M_e}{M_e} 100\% \quad (2)$$

The elastic bending moment (M_e) is typically calculated with the elastic theory, which equals 0.18PL and 0.16PL for the hogging and the sagging moment sections, respectively. Where the value of the plastic moment (M_P) is obtained from the experimental readings, which is calculated by using the experimental reaction values.

A positive sign of the moment redistribution reflects an increase in the moment at the calculated region due to redistribution from another region, whereas a negative sign indicates that the region behaved as an inverse action [19]. Table 5 shows the development of moment redistribution at different loading stages up to the ultimate load. Before cracking, at 60 kN, the redistribution was very small for all beams. After cracking and before steel yielding, at 260 kN, the effect of GFRP replacement became more evident due to its lower elastic modulus and the resulting difference in flexural stiffness between the sagging and hogging regions. For B-16-B3, the redistribution reached −14% and + 26.5% at the sagging and hogging regions, respectively, while B-16-T3 showed the opposite trend, with + 14% and −24%. After steel yielding, the redistribution increased further. At 520 kN, the corresponding values reached −20% and + 38% for B-16-B3 and + 17.5% and −27% for B-16-T3. However, the redistribution subsequently decreased as the beams approached their ultimate loads, as also observed in Figs. 13 and 14. A similar trend was reported by Araba et al. [19], where the maximum moment redistribution developed before failure and was higher than that measured at failure. At the ultimate load, as shown in Fig. 15, for control beam B-16–0, the moment redistribution value is small. This is due to using the same hogging and sagging reinforcement arrangements. This resulted in similar stiffness in both regions. For group 1, using hybrid reinforcement in the sagging moment reverses the moment redistribution from sagging to hogging moment and increases with increasing the GFRP ratio. For B-16-B1, B-16-B2 and B-16-B3, the ratios of moment redistribution at the sagging moment were −1%, −3.3%, and −8.4%, respectively. On the other hand, for group 2, using hybrid reinforcement in the hogging moment increases the moment redistribution from hogging to sagging moment with the increase in the GFRP ratio. For B-16-T1, B-16-T2 and B-16-T3, the ratios of moment redistribution at the hogging moment were −8.7%, −12.7% and −17.5%, respectively. Thus, using hybrid reinforcement at the hogging region increases the moment redistribution from the hogging to the sagging region. This behaviour is attributed to the increasing difference in flexural stiffness between the sagging and hogging regions as the GFRP replacement ratio increases, causing greater moment redistribution toward the region with higher relative stiffness

3.8. Moment capacity

The capacity of the beams was derived from the internal forces equilibrium of the section, assuming full strain compatibility. The ultimate strain and stress distributions in a typical concrete section are shown in Fig. 16, illustrating how the different stress–strain responses of steel and GFRP reinforcement were considered in the sectional analysis of the hybrid-reinforced beams. The analysis was based on the following assumptions: the maximum concrete compressive strain (ε_{cu}) was taken as 0.003 [28]; the steel reinforcement at the tension side reached the yield state; and the tensile strength contribution of the GFRP was determined according to ACI 440.1R-15 [1]. The predicted moment capacity (M_u) of the studied beams was calculated as indicated in the following procedure:

$$M_u = T_s\left(d_s - \frac{\alpha c}{2}\right) + T_f\left(d_f - \frac{\alpha c}{2}\right) + C_{s'}\left(\frac{\alpha c}{2} - d'\right) \quad (3)$$

Where

$$C_c = 0.85 \times f_c \times b \times \alpha c \quad (4)$$

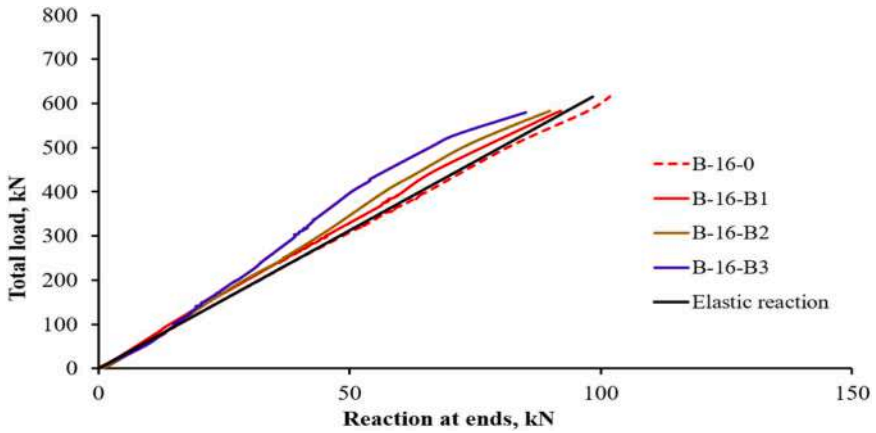


Fig. 13. Total load versus end support reactions for group 1.

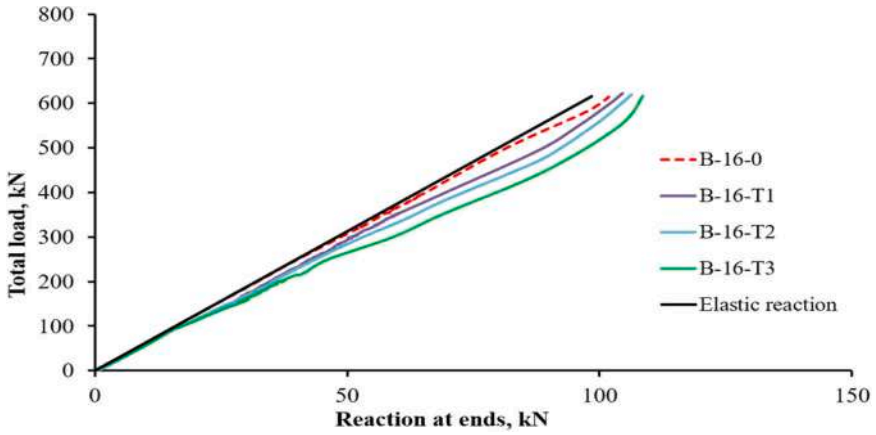


Fig. 14. Total load versus end support reactions for group 2.

$$T_s = A_s \times f_y \tag{5}$$

$$T_f = A_f \times f_f \tag{6}$$

$$C_s' = A_s' \times f_s' \tag{7}$$

$$c = \frac{T_s + T_f - C_s'}{C_c} \tag{8}$$

Where C_c is the resultant of compression stress carried by the concrete; T_s and T_f are the tensile forces of steel and GFRP reinforcement, respectively; f_f and f_y are the tensile stress of the GFRP bars and the yield stress of the steel bars, respectively; b is the section's width; d_f, d_s and d' are the depths of GFRP, steel, and compression steel bars, respectively; c is the depth of the neutral axis from the top fiber of compression; A_s and A_s' are the areas of the tension and compression steel reinforcement, respectively; A_f is the area of the GFRP reinforcement; α is the stress block factor which is considered 0.75 [1].

Table 6 presents the moment capacities of the experimental versus those predicted by the current procedure. The comparison of the test results with those obtained from the analytical model showed a good validation of the model. The ratios of experimental to analytical ranged between 1.02 and 1.01.

4. Finite-element modeling

Finite element analysis (FEA) has been extensively used to simulate complex structural systems, various materials, and stress conditions, thereby enabling comprehensive parametric studies. In this study, ABAQUS software [30] was selected to model the flexural behaviour of continuous RC beams with FRP/steel reinforcement. Moreover, a parametric investigation was performed to determine the impact of tension reinforcement ratio in hogging and sagging zones on the structure behaviors of continuous beams.

4.1. Description of the elements

The fiber-reinforced polymer (FRP) and steel bars, 2-node linear 3D link elements (T3D2) were used. This element (T3D2) is exclusively subjected to axial loads, as illustrated in Fig. 17. The 8-node brick element (C3D8R) was used to model both the concrete beam and steel loading plates. C3D8R provides three translational degrees of freedom at each node, denoted as u, v, and w, corresponding to displacements along the x, y, and z axes, respectively.

4.2. Boundary conditions, loading and interaction

As shown in Fig. 17, the boundary conditions consisted of a roller support at each end and a central hinged support. The roller support prevents movement in the direction of the X and Y axes and rotation around the Z-axis. Where, the hinged support prevents movement in all directions and rotation around the Z-axis only. As reported in previous studies [9,31] and the current experimental tests, no slippage was observed between the concrete and the GFRP or steel reinforcement. Therefore, a complete bond between the reinforcement and the concrete was considered.

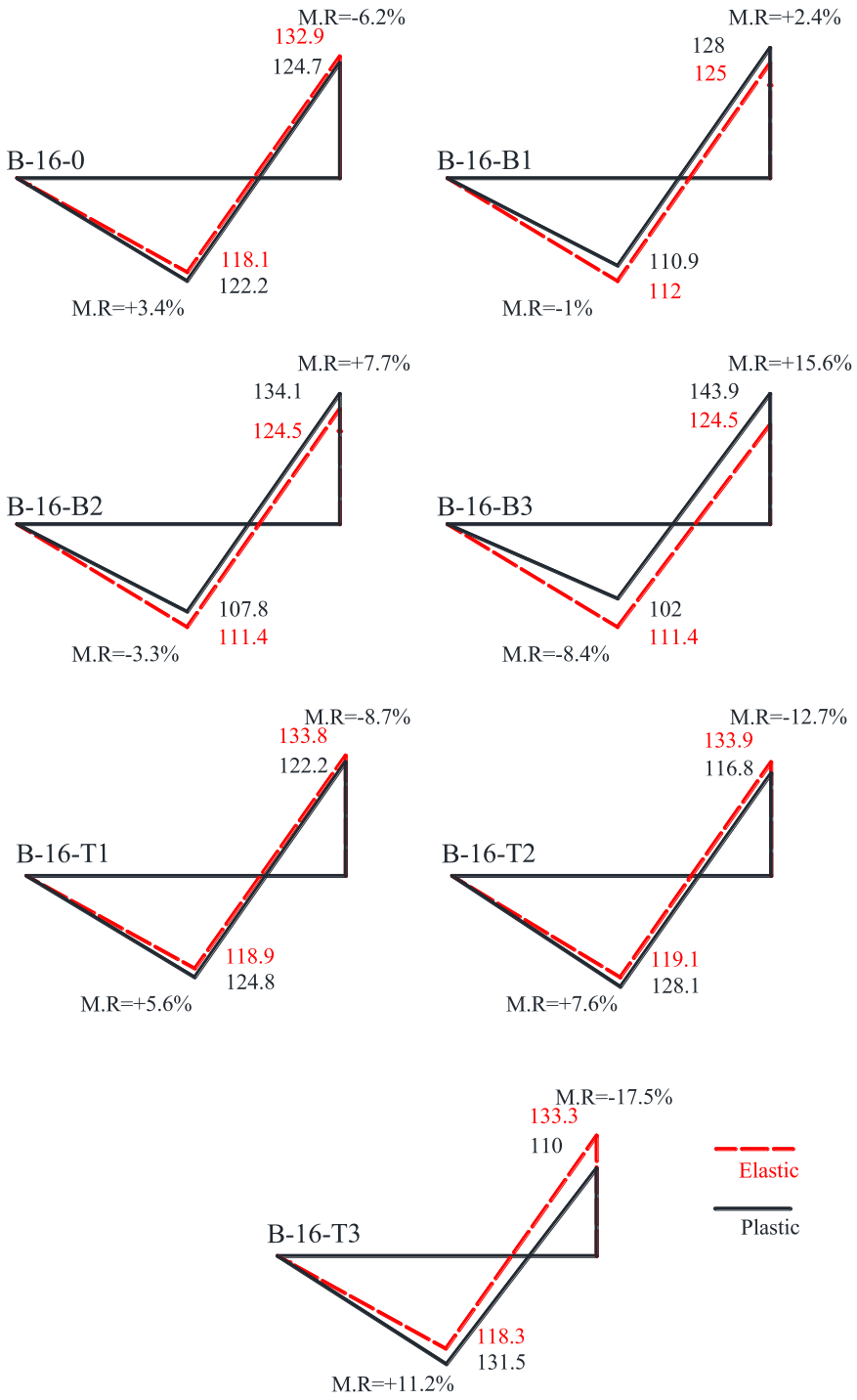


Fig. 15. Measured versus elastic bending moment diagrams.

4.3. Modeling parameters for concrete

Concrete Damage Plasticity Model (CDPM) was used to delineate the compressive and tensile properties of concrete. As reported in previous work, CDPM is able to accurately model the inelastic properties of concrete in both tension and compression zones, including damage and fracture [30]. The equations of Park and Paulay [32] were used to plot the stress-strain curve for concrete under uniaxial compression, as shown in Fig. 18a. For tensile stress-strain of concrete, the behaviour is linear before reaching the maximum tensile strength (f_{ct}). The elastic parameters modulus of elasticity (E_c) and f_{ct} can be obtained from the material experimental tests; additionally, the fracture energy (G_f) could be obtained by Eq. (9) [30]. Fig. 18b shows the post-peak uniaxial tensile stress-displacement relation. The modeling parameters of concrete are summarized in Table 7 [30]. The parameters include the ultimate compressive strain of concrete (ε_o), the crushing strain of concrete (ε_{cu}), dilation angle, Poisson's ratio (υ), biaxial to uniaxial stresses (f_{b0}/f_{c0}), eccentricity parameter, yield surface factor (K), and the viscosity parameter [9,33].

$$G_f = 110\left(\frac{f_{cy}}{10}\right)^{0.18} \text{Jole} \Big/ \text{m2} \tag{9}$$

Where G_f = fracture energy; Jole/m^2 = 0.001 MPa.

Table 5
Moment redistribution ratios at different loading stages for the experimental specimens.

Beam notation	Moment redistribution ratio before cracking at load 60 kN (β%)		Moment redistribution ratio after cracking and before yielding at 260 kN (β%)		Moment redistribution ratio after yielding at load 520 kN (β%)		Moment redistribution ratio at failure load (β%)	
	Sagging	Hogging	Sagging	Hogging	Sagging	Hogging	Sagging	Hogging
B-16–0	0.1	-0.28	0.38	-0.55	2.3	-4.5	3.4	-6.2
B-16-B1	-0.2	0.7	-3	7	-3.5	7.8	-1	2.4
B-16-B2	-1	1.5	-7.5	13.2	-8.5	14.6	-3.3	7.7
B-16-B3	0.3	-1.2	-14	26.5	-20	38	-8.4	15.6
B-16-T1	0.3	-0.6	7	-12.4	9.1	-16	5.6	-8.7
B-16-T2	0.2	-0.3	9.2	-16.5	11	-22	7.6	-12.7
B-16-T3	0.2	-0.3	14	-24	17.5	-27	11.2	-17.5

β = Moment redistribution ratio = $(M_P\text{-}M_E)/M_E$.

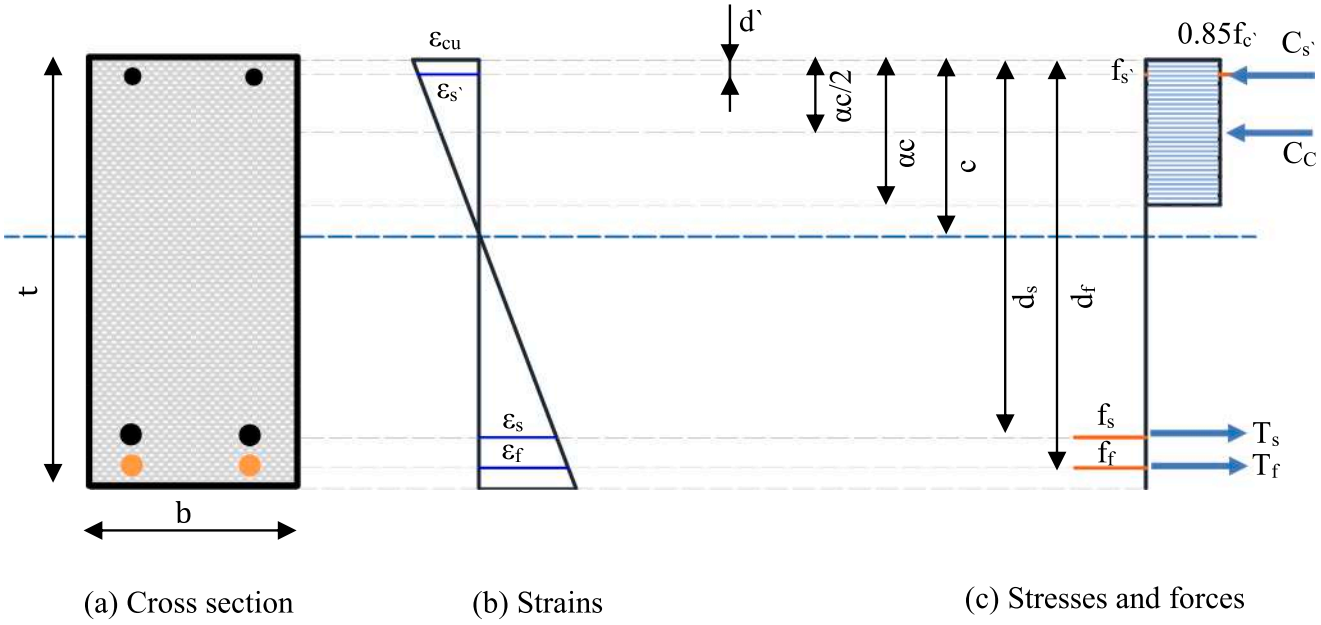


Fig. 16. Strain, stresses and forces of a reinforced concrete section.

Table 6
Comparison between the predicted and experimental moment capacities of the tested beams.

M_{Exp} / M_{Pre}		Predict moment at failure, M_{pre} (ACI)		Experimental moment at failure, M_{exp}		Experimental Failure load	Specimens
Hogging	Sagging	Hogging	Sagging	Hogging	Sagging	P_{Exp}	
0.97	1.00	127	122.6	123.2	122.9	614	B-16–0
1.04	1.01	123.2	110.3	128	110.9	585	B-16-B1
1.10	1.02	122.07	105.7	134.1	107.8	583	B-16-B2
1.18	0.99	122	103.2	143.9	102	580	B-16-B3
0.98	1.01	124.8	122.6	122.2	125.5	622	B-16-T1
0.92	1.04	126.5	122.6	116.8	128.1	620	B-16-T2
0.86	1.07	128.5	122.6	110	131.5	616	B-16-T3
1.01	1.02	Average					
0.11	0.027	Standard deviation					
11.3%	2.6%	Coefficient of Variation					

4.4. Modeling parameters of GFRP and steel reinforcement

The behaviour of both steel and GFRP reinforcing bars was defined according to their experimental test results. As shown in Fig. 19, a bilinear elastoplastic model was adopted for steel reinforcement. At the elastic stage, the elastic modulus (E_s) of steel is considered to be 200 GPa, while at the plastic stage, the steel modulus is assumed to be 0.1 E_s. As for the GFRP bars, the stress-strain relationship of GFRP bars is linear elastic up to rupture, as shown in Fig. 20. The used Poisson's ratio and Elastic modulus were 0.25 and 55 GPa, respectively.

4.5. Validation of FEM results with the test outputs

The FE model was validated by comparing the numerical results with the experimental results in terms of failure load, deflection, ductility, moment redistribution, load–deflection response, end reactions, and failure behaviour. Table 8 compares the experimental and numerical results for all tested beams. Good agreement was obtained, with average experimental-to-numerical ratios of 0.99, 0.95, 0.96, and 0.95 for failure load, deflection, ductility, and moment redistribution, respectively. These results indicate that the FE model reasonably reproduced the overall response of the tested beams. Further validation was carried out

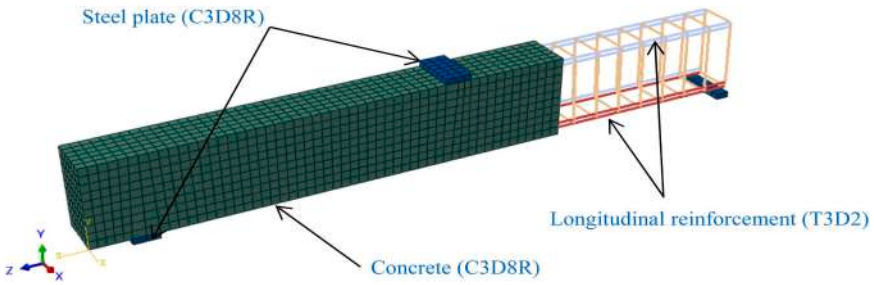
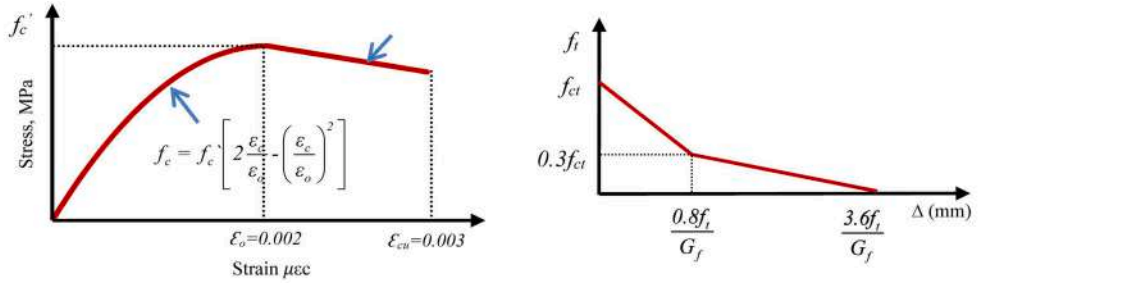


Fig. 17. Elements utilized in the finite element model.



(a) Uniaxial compressive stress-strain graph for concrete (b) Post-peak uniaxial tensile stress-displacement relation

Fig. 18. Performance of concrete to uniaxial loading.

Table 7
Parameters for configuring the CDPM.

parameters	Value
ε_o	0.2%
ε_{cu}	0.3%
υ	0.2
Dilation angle	37°
Eccentricity parameter	0.10
f_{b0}/f_{c0}	1.16
Shape factor for yield surface, K	0.667
Viscosity parameter	0

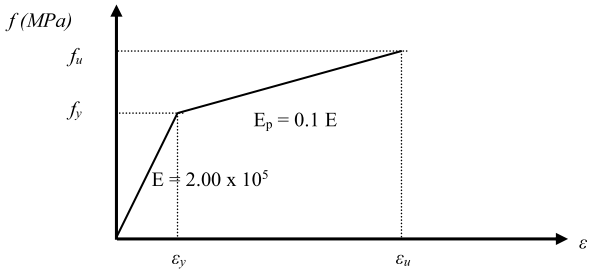


Fig. 19. Idealized stress-strain curve for steel reinforcement.

using two representative beams, B-16-B1 and B-16-T1, representing GFRP replacement in the sagging and hogging regions, respectively. As shown in Fig. 21(a), the experimental and numerical load–deflection responses were in good agreement throughout the loading stages. The comparison of the end reactions in Fig. 21(b) also showed good agreement, indicating that the FE model reasonably reproduced the development of the internal force distribution during loading. In addition, the experimentally observed crack patterns were compared with the concrete plastic strain distributions obtained from the FE analysis for the same beams, as shown in Fig. 22. Since the FE results represent the localization of plastic strains in the concrete rather than discrete

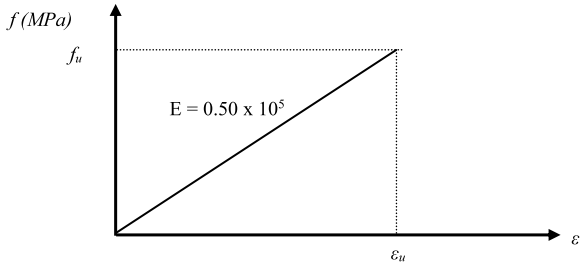


Fig. 20. Idealized stress-strain curve for GFRP reinforcement.

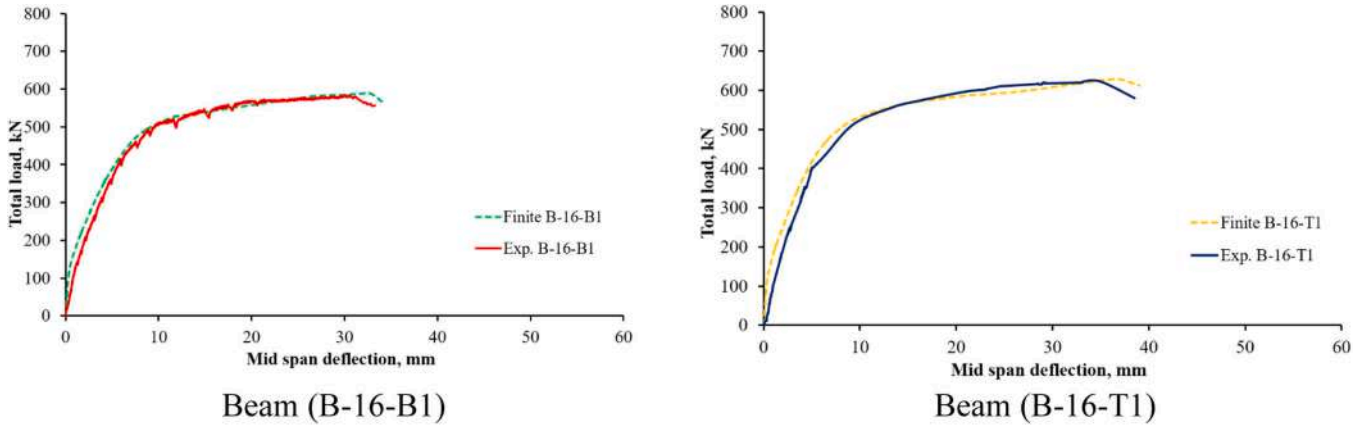
physical cracks, an exact match with the experimental crack pattern is not expected. However, the main regions of plastic strain concentration were generally consistent with the experimentally observed cracking regions. Overall, these comparisons show that the developed FE model can reasonably reproduce the main experimental response and can be used for the subsequent parametric study

4.6. Parametric study

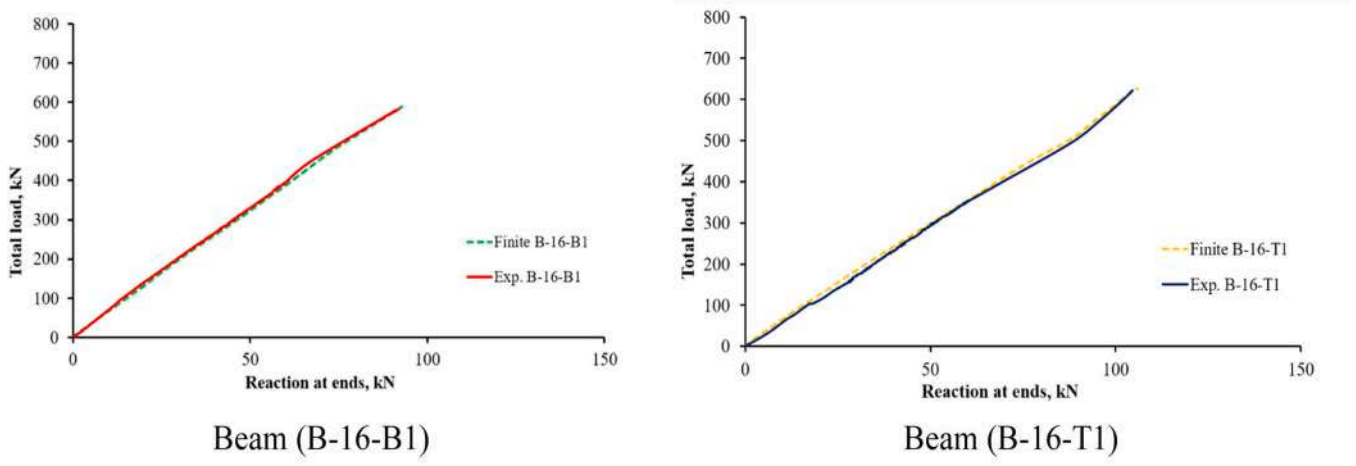
Based on the validated FE model, a parametric investigation was performed to explore the effect of new parameters. The parameters for the FE simulated beams are shown in Table 1. The parameters are the reinforcement ratio in the sagging and hogging moments and the effect of the simultaneous use of the hybrid reinforcement in both sagging and hogging regions. In addition, two FE models, B-16-B4 and B-16-T4, were analyzed to extend the GFRP replacement ratio to 100% at the selected moment region. In B-16-B4, 100% GFRP replacement was applied in the sagging moment region, while in B-16-T4, 100% GFRP replacement was applied in the hogging moment region. These models were included to investigate the response at the upper limit of the GFRP replacement ratio and to provide a numerical comparison with the hybrid-reinforced beams.

Table 8
Comparison of the experimental and numerical results for the tested beams.

Moment redistribution ratio at sagging (β%)			Deflection-based ductility (μΔ)			Deflection at failure (mm)			Failure load (kN)			Specimens
$M.R_{Exp}/M.R_{FE}$	$M.R_{FE}$	$M.R_{Exp}$	$\mu\Delta_{Exp}/\mu\Delta_{FE}$	$\mu_{\Delta FE}$	$\mu_{\Delta Exp}$	Δ_{Exp}/Δ_{FE}	Δ_{FE}	Δ_{Exp}	P_{Exp}/P_{FE}	P_{FE}	P_{Exp}	
0.92	+ 3.7	+ 3.4	0.98	5.9	5.8	0.96	37.6	36	0.99	620	614	B-16–0
0.95	-1.05	-1	0.98	5.8	5.7	0.96	33.5	32	0.99	588	585	B-16-B1
0.94	-3.5	-3.3	0.95	5.2	4.9	0.95	32	30.5	1.01	575.5	583	B-16-B2
0.95	-8.97	-8.4	0.96	4.2	4	0.95	31	29.5	1.01	574	580	B-16-B3
0.95	+ 5.9	+ 5.6	0.96	6	5.75	0.92	37	34	0.99	627	622	B-16-T1
0.94	+ 8.1	+ 7.6	0.95	5.8	5.5	0.93	35	32.5	1.01	612	620	B-16-T2
0.97	+ 11.5	+ 11.2	0.92	5.4	4.95	0.95	32.8	31	1.02	600	616	B-16-T3



a the experimental and FE load–deflection responses for the selected beams.



b the experimental and FE end reactions for the selected beams.

Fig. 21. Comparison between the experimental and FE results for the representative beams.

4.7. Numerical study results

4.7.1. Modes of failure

Fig. 23 shows the FE failure modes of the analyzed beams, where B-16-B4 and B-16-T4 represent extensions of Groups 1 and 2, respectively, by increasing the GFRP replacement ratio to 100% at the corresponding moment regions. It should be noted that the FE results represent the localization of plastic strains in the concrete rather than discrete physical cracks. Therefore, an exact correspondence with the experimentally observed crack pattern is not expected. Generally, the variation in reinforcement ratios slightly affected the structural response and failure behaviour of the beams. Reducing the reinforcement ratios in the sagging or hogging moments led to a clear flexural failure as depicted in groups 3 and 5. The increase in reinforcement ratio with the beams of groups 4 and 6 led to flexural shear failures, similar to groups 1 and 2. Finally, for group 7, using a similar hybrid reinforcement ratio in both sagging and hogging moments led to flexural shear failure.

4.7.2. Ultimate loads

Table 9 lists the ultimate loads of the FE studied beams. For group 3, as expected, decreasing the sagging reinforcement decreased the ultimate load compared to group 1. The ultimate loads of beams B-12-B0, B-12-B1, B-12-B2, and B-12-B3 reached 81, 84, 83, and 82% of those achieved by B-16–0, B-16-B1, B-16-B2, and B-16-B3, respectively. For

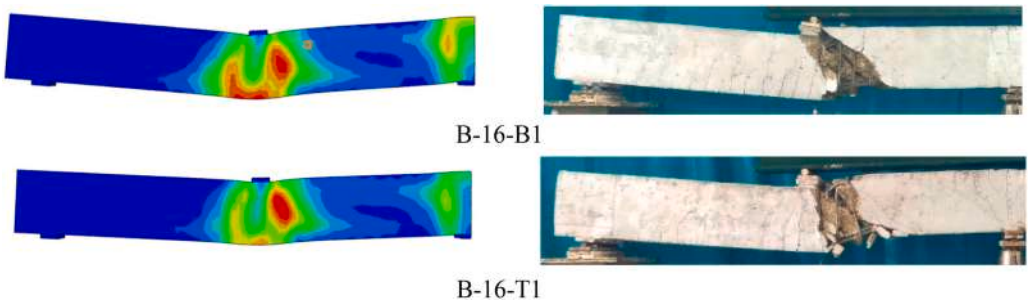


Fig. 22. Comparison between the experimental crack patterns and FE concrete plastic strain distributions for the representative beams.

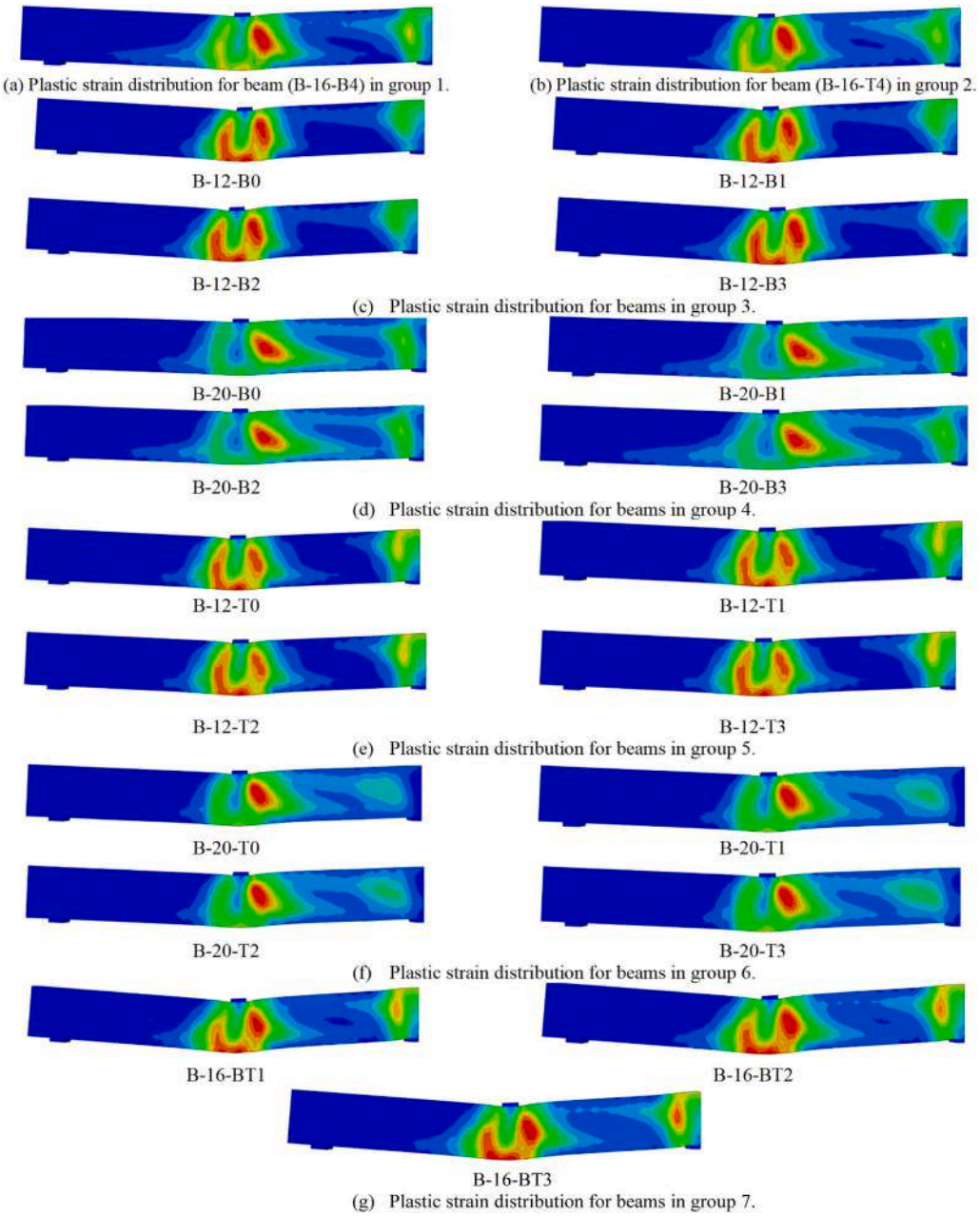


Fig. 23. Plastic strain distribution for the analyzed beams.

group 4, with the increase in the sagging reinforcement, the ultimate load increased compared to group 1. The ultimate loads of B-20-B0, B-20-B1, B-20-B2, and B-20-B3 reached 112, 114, 111, and 110% of those achieved by B-16–0, B-16-B1, B-16-B2, and B-16-B3, respectively. In contrast, the variation in hogging reinforcement had a minor effect on the ultimate load compared to group 2. For group 5, the ultimate loads of

Table 9
Summary of the analytical results.

Group No.	Beam notation	At yield load of steel at sagging		At yield load of steel at hogging		At ultimate load		μ_Δ
		P_{ys}, kN	Δ_y, mm	P_{yh}, kN	Δ_y, mm	P_{ult}, kN	Δ_{ult}, mm	
Group 3	B-12-B0	306	4.00	380	6.72	499	42.8	10.7
	B-12-B1	283	4.20	353	6.8	491.8	41	10
	B-12-B2	222	4.50	315	7.2	485	38	8.4
	B-12-B3	190	4.60	288	7.4	475	35	7.7
Group 4	B-20-B0	603	8.2	563	7.18	686	32	4.4
	B-20-B1	578	8.6	503	7.40	672	28.5	3.85
	B-20-B2	490	8.8	444	7.80	650	26.8	3.59
	B-20-B3	400	8.9	372	7.85	634	25	3.3
Group 5	B-12-T0	436	6.06	356	5.07	591.7	44	8.65
	B-12-T1	416	6.89	324	5.09	590	43.5	8.55
	B-12-T2	400	7.1	285	5.3	591	42.5	8.02
	B-12-T3	390	7.8	247	5.3	587.5	41.6	7.9
Group 6	B-20-T0	492	6.67	600	16	646	33	4.9
	B-20-T1	481	6.73	581	13.3	648	32.2	4.7
	B-20-T2	472	6.6	510	7.5	634	31.1	4.7
	B-20-T3	440	6.81	457	6.55	620	30.1	4.4
Group 7	B-16-BT1	470	6.34	430	6.0	608	34	5.69
	B-16-BT2	382	6.70	360	6.6	599	32	4.8
	B-16-BT3	332	7.7	315	7.4	580	31.5	4.2

P_{ys} = yield load for sagging steel; P_{yh} = yield load for hogging steel; P_{ult} = ultimate load; Δ *the deflection at sagging;* Δ_y = deflection at yield load; Δ_{ult} = deflection corresponding to ultimate load; μ_Δ=ductility index = Δ_{ult}/Δ_y.

beams B-12-T0, B-12-T1, B-12-T2, and B-12-T3 reached 96, 95, 95.5, and 95% of those achieved by B-16–0, B-16-T1, B-16-T2, and B-16-T3, respectively. Whereas, for group 6, increasing the hogging reinforcement caused a slight increase in the load compared to group 2. The ultimate loads of beams B-12-T0, B-12-T1, B-12-T2, and B-12-T3 reached 105, 104, 102, and 101% of those achieved by B-16–0, B-16-T1, B-16-T2, and B-16-T3, respectively. Finally, for group 7, using similar hybrid reinforcement ratios in both sagging and hogging moments resulted in ultimate loads near to those of groups 1 and 2. The ultimate loads of beams B-16-BT1, B-16-BT2, and B-16-BT3 reached 104, 102, and 100% of those achieved by B-16-B1, B-16-B2, and B-16-B3, respectively.

4.7.3. Load deflection behaviour

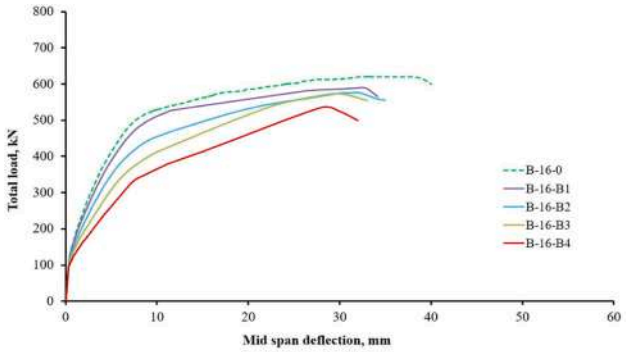
The load-deflection relationships of the FE-analyzed beams are shown in Fig. 24. The additional numerical models B-16-B4 and B-16-T4 extended the GFRP replacement ratio to 100% in the sagging and hogging moment regions, respectively. The results showed that 100% GFRP replacement had a more pronounced effect on the load-deflection response in the sagging region than in the hogging region. Groups 3 and 4 exhibited similar behaviour to group 1. For group 3, however, decreasing the sagging reinforcement by approximately 44% compared to that used in group 1 increased the average ultimate deflection by 17.7%, while decreasing the maximum load by 17.5%. Conversely, for group 4, increasing the sagging reinforcement by almost 55% compared to that used in group 1 decreased the average ultimate deflection by 10% and increased the maximum load by 12%, as detailed in Table 9. These results indicate a significant influence of the sagging reinforcement ratio on the flexural behaviour of the beams. Therefore, reducing the sagging reinforcement leads to higher deformability, resulting in increased ultimate mid-span deflection but reduced load-carrying capacity. Groups 5 and 6 showed similar behaviour to group 2. For group 5, however, decreasing the hogging reinforcement by approximately 44% in comparison to group 2 increased the average ultimate deflection by 27% and decreased the ultimate load by 5%. For group 6, increasing the hogging reinforcement by almost 55% compared to group 2 decreased the average of ultimate deflection by 6% and increased the ultimate load by 3%, as detailed in Table 8. These results a minor effect of the hogging reinforcement ratio on the deformability and overall flexural response of the specimens. Finally, using hybrid reinforcement in both the sagging and hogging moments in group 7 showed a similar behaviour to that of group 1. This confirms the experimental results; the sagging reinforcement exerts the most significant influence on the load deflection response.

4.7.4. Ductility

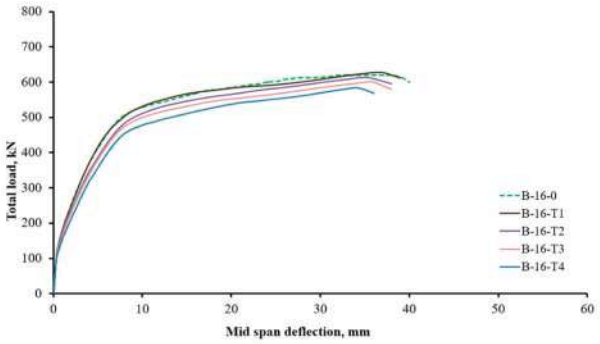
4.7.4.1. Deflection-based ductility (μ_Δ). The FE ductility indices ($\mu\Delta = \frac{\Delta u}{\Delta y}$) for the analyzed beams are listed in Table 9. For group 3, decreasing the sagging reinforcement increased the ductility index compared to group 1, as evidence for beam B-12-B1, which showed a ductility value about 75% higher than that of B-16-B1. This behavior can be attributed to lower reinforcement ratios, which allow gradual steel yielding and better strain redistribution, leading to higher ductility. For group 4, increasing the sagging reinforcement decreased the ductility index relative to group 1, with beam B-20-B1 exhibiting a ductility index 33% lower than that of beam B-16-B1. The higher sagging reinforcement ratios limit strain development in the tensile zone, increase stiffness at the primary stages, and consequently reduce the ductile performance of the beam. Additionally, within each group, increasing the GFRP ratio reduced the ductility. In contrast, the variation in hogging reinforcement had a lower influence on the ductility index. For group 5, decreasing the hogging reinforcement increased the ductility index compared to group 2, as observed for beam B-12-T1, which exhibited 49% higher ductility than that of beam B-16-B1. Whereas, for group 6, increasing the hogging reinforcement decreased the ductility index relative to group 2, with beam B-20-T1 exhibiting 18% lower ductility than that of beam B-16-T1. This trend can be attributed to mechanisms similar to those observed in previous groups. Finally, for group 7, the hybrid reinforcement in both the sagging and hogging moments showed a similar behaviour to that of group 1. Thus, the sagging reinforcement exerts a clear influence on the ductility compared to the hogging reinforcement.

4.7.5. Moment redistribution

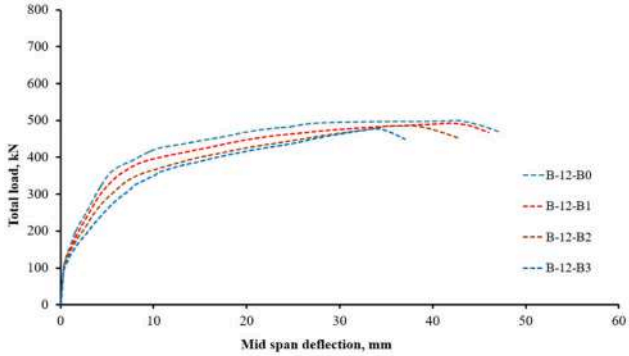
The moment redistribution for the FE analyzed beams is presented in Table 10. The values of the moment redistribution at ultimate loads were calculated by Eq. [2]. For the additional numerical models, extending the GFRP replacement ratio to 100% resulted in moment redistribution ratios of −11.6% and + 21.7% at the sagging and hogging regions, respectively, for B-16-B4. For B-16-T4, the corresponding values were- + 14.4% and −26.1%, respectively. These results confirm that increasing the GFRP replacement ratio increases the moment redistribution from the GFRP-reinforced region toward the steel-reinforced



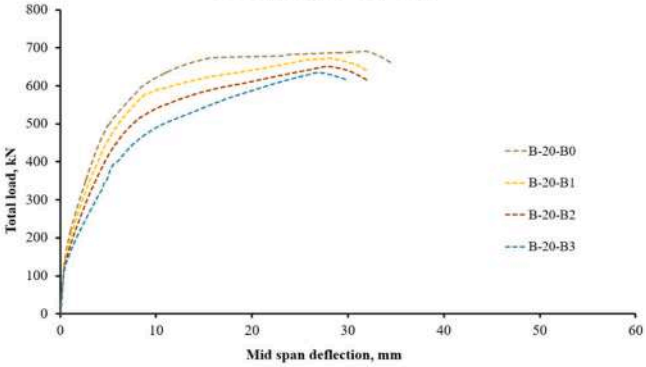
(a) Total load-midspan deflection curve for group 1 including B-16-B4.



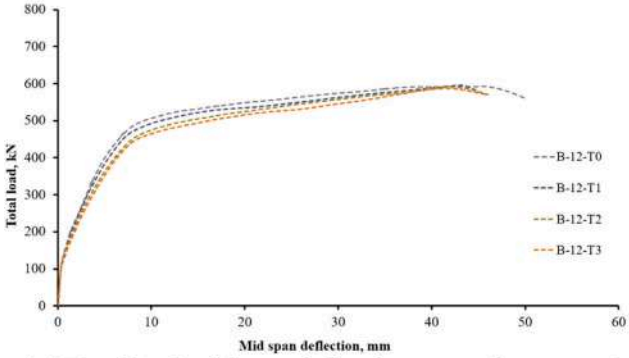
(b) Total load-midspan deflection curve for group 2 including B-16-T4.



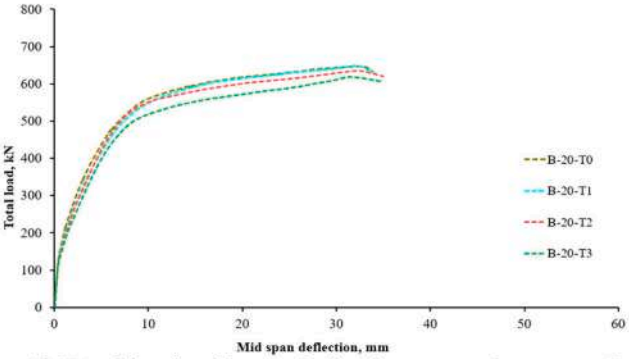
(c) Total load-midspan deflection curve for group 3.



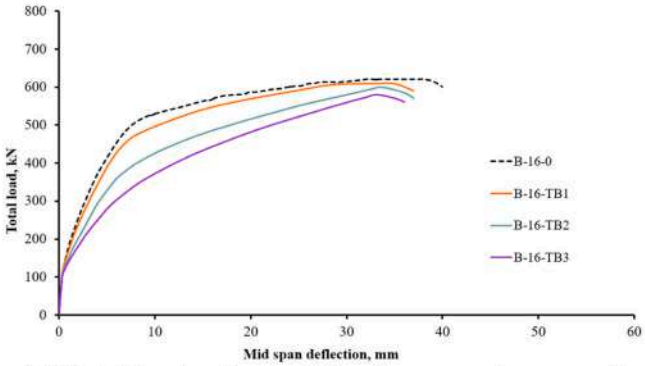
(d) Total load-midspan deflection curve for group 4.



(e) Total load-midspan deflection curve for group 5.



(f) Total load-midspan deflection curve for group 6.



(g) Total load-midspan deflection curve for group 7.

Fig. 24. Load versus mid-span deflection for the analyzed beams.

Table 10
Moment redistribution ratios for the analyzed beams.

Group No.	Beam notation	Plastic moment (kN.m)		Elastic moment (kN.m)		Moment redistribution ratio (β%)	
		Sagging	Hogging	Sagging	Hogging	Sagging	Hogging
Group 1	B-16-B4	88.4	140	100	115	-11.6	21.7
Group 2	B-16-T4	128	93	111.9	125.9	14.4	-26.1
Group 3	B-12-B0	77	135.7	92.7	104.3	-16.9	30
	B-12-B1	73.96	142.9	93.1	104.7	-20.5	36.5
	B-12-B2	70.7	149.6	93.1	104.7	-24	42.3
	B-12-B3	61.6	163.6	91.8	103.3	-32.9	58.5
Group 4	B-20-B0	164.2	132.4	147.5	165.9	11.3	-20.2
	B-20-B1	140.1	122.9	129	145.2	8.6	-15.3
	B-20-B2	130.6	128.8	124.8	140.4	4.7	-8.2
	B-20-B3	114	152.5	121.8	137	-6.4	11.3
Group 5	B-12-T0	129.3	96.4	113.6	127.8	13.8	-24.6
	B-12-T1	133.6	89.7	114.2	128.5	16.9	-30.2
	B-12-T2	135.8	83.6	113.5	127.7	19.4	-34.5
	B-12-T3	137.8	76.8	112.8	126.9	22.2	-39.5
Group 6	B-20-T0	119.8	147.9	124	139.5	-3.4	6
	B-20-T1	123.5	141.7	124.4	139.6	-0.7	1.3
	B-20-T2	125.1	130.5	121.8	137.1	2.7	-4.8
	B-20-T3	127.5	116.3	118.8	133.7	7.3	13-
Group 7	B-16-BT1	121.5	121.07	116.5	131.1	4.3	-7.6
	B-16-BT2	119.7	119.9	115.01	129.4	4.1	-7.1
	B-16-BT3	114.9	117.9	111.3	125.2	3.3	-5.9

β = Moment redistribution ratio = $(M_P\text{-}M_E)/M_E$.

region due to the reduction in relative flexural stiffness. For group 3, decreasing the sagging reinforcement reversed the moment redistribution and increased the transmission of moment from sagging to hogging moment compared to group 1. At the sagging region, the moment redistribution value of B-12-B2 was approximately six times that of B-16-B2. This behaviour is attributed to the reduction in sagging reinforcement, which decreased flexural stiffness and promoted moment redistribution toward the hogging moment. In contrast, for group 4, increasing the sagging reinforcement decreased the moment redistribution from sagging to hogging moment compared to group 1. At the sagging region, B-20-B2 showed a moment redistribution ratio approximately 42.4% higher than B-16-B2. This behaviour is attributed to the increase in sagging reinforcement, which significantly improved the flexural stiffness and constrained the transfer of moment from sagging to hogging moment. However, with increasing GFRP reinforcement, the sagging moment redistribution changed from a gained moment to a redistributed moment, reflecting the reduced stiffness associated with increasing GFRP ratio. For group 5, decreasing the hogging reinforcement enhanced the moment redistribution from hogging to sagging moment compared to group 2. At the hogging zone, B-12-T2 demonstrated a moment redistribution ratio about 171% higher than B-16-T2. This result is mainly ascribed to the reduced flexural stiffness related to lower hogging reinforcement. Conversely, for group 6, increasing the hogging reinforcement decreased the moment redistribution from hogging to sagging moment relative to group 2. At the hogging zone, B-20-T2 exhibited a moment redistribution ratio approximately 62% lower than that of B-16-T2. This behaviour is attributed to increased hogging reinforcement, resulting in higher flexural stiffness and reduced moment redistribution from hogging to sagging moment. Finally, for group 7, using the same hybrid reinforcement in both the sagging and hogging regions had a slight effect on the moment redistribution when compared to beam B-16–0.

5. Conclusions

This study examined the flexural behaviour of two-span RC beams with steel or hybrid GFRP/steel tension reinforcement. An experimental study on seven beams and FE analysis on fifteen beams were conducted. The studied parameters were the GFRP replacement location and ratio, and the tension reinforcement ratio. Based on the experimental and FE analysis, the following conclusions are summarized:

- The use of hybrid reinforcement in sagging or hogging moment regions affected the load deflection response; however, the effect was more significant when the hybrid reinforcement was used in the sagging moment, where the beams reached the allowable service deflection at lower load levels compared to the control beam. This behaviour is attributed to the lower elastic modulus of GFRP, which reduced the post-cracking flexural stiffness of the sagging region and consequently increased the beam deflection.
- The beams with hybrid reinforcement in the sagging moment showed lower ductility values compared to those with hybrid reinforcement in the hogging moment, which showed a limited effect compared with the control beam. At 75% GFRP replacement, the ductility index decreased from 5.8 for the control beam to 4.0 and 4.95 for GFRP replacement in the sagging and hogging regions, respectively. This reduction was mainly associated with the earlier yielding of the remaining steel reinforcement as the GFRP replacement ratio increased.
- Using hybrid reinforcement in the sagging moment region had a more significant effect on crack width than using hybrid reinforcement in the hogging moment region. For GFRP replacement ratios of 25%, 50%, and 75%, the allowable crack width was reached at 0.71Pu, 0.60Pu, and 0.48Pu, respectively, compared with 0.77Pu, 0.72Pu, and 0.63Pu for the corresponding beams with hybrid reinforcement in the hogging moment region. This behaviour is mainly attributed to the lower post-cracking flexural stiffness resulting from the lower elastic modulus of GFRP.
- The location of the hybrid reinforcement affected the moment redistribution. When GFRP was used in the hogging moment region, the moment redistribution from the hogging to the sagging region increased with the GFRP replacement ratio and reached 17.5% at 75% replacement. In contrast, using GFRP in the sagging moment region reversed the direction of moment redistribution, reaching 8.4% from the sagging to the hogging region at 75% replacement. This behaviour was mainly related to the difference in flexural stiffness between the sagging and hogging regions.
- Decreasing the sagging or hogging reinforcement reduced the load capacity and enhanced the ductility. Specifically, the ultimate load decreased by an average of 17.5% and 5% for reductions in sagging and hogging reinforcement, respectively, while the ductility increased significantly by approximately 80% and 53%, respectively.

- Reducing the reinforcement in either the sagging or hogging region increased the moment redistribution toward the opposite region, with the effect becoming more noticeable as the GFRP replacement ratio increased. The moment redistribution of B-12-B2 was approximately six times that of B-16-B2 due to the lower flexural stiffness of the sagging region.

This research is designed to study the behaviour of continuous two span beams with hybrid reinforcement. It is worth mentioning that the drawn conclusions are limited to the conditions of the study in terms of the beams' dimensions, the studied parameters, and the properties of the used materials. In addition, as customary in all research work, future studies are needed to cover many parameters that have not been studied yet (e.g., the effect of concrete type and strength, length-to-depth ratio, and type of FRP reinforcement).

CRediT authorship contribution statement

Nesreen M. Kassem: Supervision. **Abdelaziz Nabil:** Writing – original draft, Formal analysis, Data curation. **Ibrahim Abdelhakim:** Writing – original draft, Resources, Data curation. **Ali Hassan:** Writing – review & editing, Writing – original draft, Supervision, Methodology, Formal analysis, Data curation, Conceptualization. **Mahmoud A. Abd-Elaziz:** Supervision.

Declaration of Competing Interest

The authors declare that they have no known competing financial interests or personal relationships that could have appeared to influence the work reported in this paper.

Data availability

Data will be made available on request.

References

[1] ACI 440.1R-15. Guide Des Constr Struct Concr Reinf FRP bars 2015.
[2] Gunes O, Lau D, Tuakta C, Büyüköztürk O. Ductility of FRP–concrete systems: investigations at different length scales. Constr Build Mater 2013;49:915–25. https://doi.org/10.1016/j.conbuildmat.2012.10.017.
[3] Ribeiro SE, Diniz SM. Reliability-based design recommendations for FRP-reinforced concrete beams. Eng Struct 2013;52:273–83. https://doi.org/10.1016/j.engstruct.2013.02.026.
[4] Wan C, Li C, Zhu H, Zheng Y, Cheng S. Serviceability evaluation model of SFRC beams reinforced with FRP bars based on deformation control. 104807 Structures 2023;56:104807. https://doi.org/10.1016/j.istruc.2023.06.138.
[5] Adam MA, Said M, Mahmoud AA, Shanour AS. Analytical and experimental flexural behavior of concrete beams reinforced with glass fiber reinforced polymers bars. Constr Build Mater 2015;84:354–66. https://doi.org/10.1016/j.conbuildmat.2015.03.057.
[6] Gravina RJ, Smith ST. Flexural behaviour of indeterminate concrete beams reinforced with FRP bars. Eng Struct 2008;30(9):2370–80. https://doi.org/10.1016/j.engstruct.2007.12.019.
[7] El Refai A, Abed F, Al-Rahmani A. Structural performance and serviceability of concrete beams reinforced with hybrid (GFRP and steel) bars. Constr Build Mater 2015;96:518–29. https://doi.org/10.1016/j.conbuildmat.2015.08.063.
[8] Yoo DY, Banthia N, Yoon YS. Flexural behavior of ultra-high-performance fiber-reinforced concrete beams reinforced with GFRP and steel rebars. Eng Struct 2016;111:246–62. https://doi.org/10.1016/j.engstruct.2015.12.003.
[9] Bencardino F, Condello A, Ombres L. Numerical and analytical modeling of concrete beams with steel, FRP and hybrid FRP-steel reinforcements. Compos Struct 2016;140:53–65. https://doi.org/10.1016/j.compstruct.2015.12.045.
[10] Qu W, Zhang X, Huang H. Flexural behavior of concrete beams reinforced with hybrid (GFRP and steel) bars. J Compos Constr 2009;13(5):350–9. https://doi.org/10.1061/(ASCE)CC.1943-5614.0000035.
[11] Mustafa SA, Hassan HA. Behavior of concrete beams reinforced with hybrid steel and FRP composites. HBRC J 2018;14(3):300–8. https://doi.org/10.1016/j.hbrcj.2017.01.001.
[12] Ge W, Zhang J, Cao D, Tu Y. Flexural behaviors of hybrid concrete beams reinforced with BFRP bars and steel bars. Constr Build Mater 2015;87:28–37. https://doi.org/10.1016/j.conbuildmat.2015.03.113.
[13] Lau D, Pam HJ. Experimental study of hybrid FRP reinforced concrete beams. Eng Struct 2010;32(12):3857–65. https://doi.org/10.1016/j.engstruct.2010.08.028.
[14] Thamrin R, Zaidir Z, Iwanda D. Ductility estimation for flexural concrete beams longitudinally reinforced with hybrid FRP–steel bars. Polymers 2022;14(5):1017. https://doi.org/10.3390/polym14051017.
[15] Tarawneh A, Alajarmeh O, Alawadi R, Amirah H, Alramadeen R. Database evaluation and reliability calibration for flexural strength of hybrid FRP/steel-RC Beams. 117758 Compos Struct 2024;329:117758. https://doi.org/10.1016/j.compstruct.2023.117758.
[16] Zhou B, Wu R, Lu S, Yin S. A general numerical model for predicting the flexural behavior of hybrid FRP-steel reinforced concrete beams. 112293 Eng Struct 2021;239:112293. https://doi.org/10.1016/j.engstruct.2021.112293.
[17] Qin R, Zhou A, Lau D. Effect of reinforcement ratio on the flexural performance of hybrid FRP reinforced concrete beams. Compos Part B Eng 2017;108:200–9. https://doi.org/10.1016/j.compositesb.2016.09.054.
[18] Ruan X, Lu C, Xu K, Xuan G, Ni M. Flexural behavior and serviceability of concrete beams hybrid-reinforced with GFRP bars and steel bars. 111772 Compos Struct 2020;235:111772. https://doi.org/10.1016/j.compstruct.2019.111772.
[19] Araba AM, Zinkaah OH, Alhawat M, Ashour A. Experimental tests of two span continuous concrete beams reinforced with hybrid GFRP-Steel bars. Structures 2023;47:2485–500. https://doi.org/10.1016/j.istruc.2022.12.055.
[20] Araba AM, Ashour AF. Flexural performance of hybrid GFRP-Steel reinforced concrete continuous beams. Compos Part B Eng 2018;154:321–36. https://doi.org/10.1016/j.compositesb.2018.08.077.
[21] Almahmood H, Ashour A, Sheehan T. Flexural behaviour of hybrid steel-GFRP reinforced concrete continuous T-beams. 112802 Compos Struct 2020;254:112802. https://doi.org/10.1016/j.compstruct.2020.112802.
[22] Akiel MS, El-Maaddawy T, El Refai A. Serviceability and moment redistribution of continuous concrete members reinforced with hybrid steel-BFRP bars. Constr Build Mater 2018;175:672–81. https://doi.org/10.1016/j.conbuildmat.2018.04.202.
[23] Abushanab A, Alnahhal W, Farraj M. Structural performance and moment redistribution of basalt FRC continuous beams reinforced with basalt FRP bars. 112390 Eng Struct 2021;240:112390. https://doi.org/10.1016/j.engstruct.2021.112390.
[24] Modabber-Saeed A, Lotfollahi-Yaghin MA, Maleki A. Moment redistribution in Hybrid-RC continuous beams with T-section using FEM. Structures 2023;54:587–95. https://doi.org/10.1016/j.istruc.2023.05.063.
[25] Kara IF, Ashour AF, Köroğlu MA. Flexural behavior of hybrid FRP/steel reinforced concrete beams. Compos Struct 2015;129:111–21. https://doi.org/10.1016/j.compstruct.2015.03.073.
[26] West Conshohocken, PA, USA: Annual Book of ASTM Standards; 2021.
[27] ASTM E8/E8M-22. Standard Test Methods for Tension Testing of Metallic Materials. West Conshohocken, PA, USA: Annual Book of ASTM Standards; 2022.
[28] A.C.I. Committee, "Building code requirements for structural concrete (ACI 318-19) and commentary," 2019.
[29] The Egyptian Code for Design and Construction of Reinforced Concrete Structures, ECP 203–2025, Ministry of Housing, Egypt.
[30] ABAQUS / CAE User ' s Manual.
[31] Xingyu G, Yiqing D, Jiwang J. Flexural behavior investigation of steel-GFRP hybrid-reinforced concrete beams based on experimental and numerical methods. 110117 Eng Struct 2020;206:110117. https://doi.org/10.1016/j.engstruct.2019.110117.
[32] Park R, Paulay T. Reinforced Concrete Structures. John Wiley & Sons; 1991.
[33] Hillerborg A, Modéer M, Petersson PE. Analysis of crack formation and crack growth in concrete by means of fracture mechanics and finite elements. Cem Concr Res 1976;6(6):773–81. https://doi.org/10.1016/0008-8846(76)90007-7.